



Cold Pools and Their Influence on the Tropical Marine Boundary Layer

SIMON P. DE SZOEKE AND ERIC D. SKYLLINGSTAD

College of Earth, Ocean, and Atmospheric Sciences, Oregon State University, Corvallis, Oregon

PAQUITA ZUIDEMA AND ARUNCHANDRA S. CHANDRA

Rosenstiel School of Marine and Atmospheric Science, University of Miami, Miami, Florida

(Manuscript received 19 September 2016, in final form 29 December 2016)

ABSTRACT

Cold pools dominate the surface temperature variability observed over the central Indian Ocean (0° , 80°E) for 2 months of research cruise observations in the Dynamics of the Madden–Julian Oscillation (DYNAMO) experiment in October–December 2011. Cold pool fronts are identified by a rapid drop of temperature. Air in cold pools is slightly drier than the boundary layer (BL). Consistent with previous studies, cold pools attain wet-bulb potential temperatures representative of saturated downdrafts originating from the lower midtroposphere.

Wind and surface fluxes increase, and rain is most likely within the ~ 20 -min cold pool front. Greatest integrated water vapor and liquid follow the front. Temperature and velocity fluctuations shorter than 6 min achieve 90% of the surface latent and sensible heat flux in cold pools. The temperature of the cold pools recovers in about 20 min, chiefly by mixing at the top of the shallow cold wake layer, rather than by surface flux.


Analysis of conserved variables shows mean BL air is composed of 51% air entrained from the BL top (800 m), 22% saturated downdrafts, and 27% air at equilibrium with the ocean surface. The number of cold pools, and their contribution to the BL heat and moisture, nearly doubles in the convectively active phase compared to the suppressed phase of the Madden–Julian oscillation.

1. Introduction

Atmospheric cold pools generated by convection dominate the surface air temperature variability in deep convective tropical open-ocean regions, such as the central Indian Ocean. They are observed in time series from the Dynamics of the Madden–Julian Oscillation (DYNAMO) experiment in the southern intertropical convergence zone (ITCZ; Yokoi et al. 2014), at the equatorial Maldives (Feng et al. 2015), and on the equator at 80°E (de Szoeke et al. 2015; de Szoeke and Edson 2017). A basic mechanistic understanding of cold pools relates them to their parent convection: cold pools form when cloud or rainwater evaporates into air. The air

may be first cooled through evaporation of cumulus cloud by dry environmental air entrained into updrafts (e.g., LeMone and Zipser 1980; Lucas et al. 1994). Evaporation of rain or cloud conserves wet-bulb potential temperature θ_w or equivalent potential temperature θ_e . Continued evaporation generates a negative buoyancy capable of accelerating the air downward, forming a downdraft. Continued evaporative cooling and moistening by rain keeps the downdraft nearly saturated when it reaches the planetary boundary layer (BL), where it spreads horizontally along the surface in a cold pool (Zipser 1977).

Cold pools have become a topic of renewed fascination because of their potential role in assisting the shallow-to-deep convective transition (e.g., Rowe and Houze 2015) and to correct erroneous convective diurnal cycles in models (e.g., Rio et al. 2009; Schlemmer and Hohengger 2014). Improved modeling combined with precise remote sensing provides new insights into the relative strengths of varying cold pool processes (e.g., Feng et al. 2015). Basic near-surface observations of cold pool properties complement these perspectives from modeling.

 Denotes content that is immediately available upon publication as open access.

Corresponding author e-mail: S. P. de Szoeke, sdeszoek@ceoaas.oregonstate.edu

DOI: 10.1175/JAS-D-16-0264.1

© 2017 American Meteorological Society. For information regarding reuse of this content and general copyright information, consult the [AMS Copyright Policy](#) (www.ametsoc.org/PUBSReuseLicenses).

The tropical BL is a reservoir of moist static energy that drives cumulus convection. Its temperature and humidity determine the conditional buoyancy of a cumulus parcel throughout the troposphere, so they have a strong influence on convective available potential energy (CAPE), the energy that could be extracted by moist convection. The processes regulating BL moist static energy are thus important for convective schemes (e.g., Arakawa and Schubert 1974; Zhang and McFarlane 1995; Raymond 1994), and recent work examines the relative roles of boundary layer–top entrainment drying versus cumulus updrafts/downdrafts on the BL thermodynamic budget (Thayer-Calder and Randall 2015). Surface sensible and evaporative latent heat fluxes (80%–90% is latent heat) are the source of the BL moist static energy. Turbulent entrainment and cumulus updrafts and downdrafts are its sinks.

Marine cold pools were observed at the surface from the Research Vessel (R/V) *Roger Revelle* stationed in the central Indian Ocean (0°, 80°E) for most of two research cruise legs during the DYNAMO field campaign. The DYNAMO experiment (Yoneyama et al. 2013; Johnson and Ciesielski 2013; Moum et al. 2014; de Szoeke et al. 2015) documented the evolution of the structure and energy budgets of the atmosphere and upper ocean, of the interactions between the atmosphere and ocean, and of the convective population during the passage of two intraseasonal Madden–Julian oscillation (MJO) convective events. This study focuses on the statistics of convective cold pools and their effect on atmosphere–ocean interactions, as observed from the *Revelle*. Their effect will also be analyzed as a function of intraseasonally changing convection.

Cold pools show a rapid reduction of air temperature, followed by a slow recovery, in 1-min surface time series from the equator at 80°E. The observations are consistent with cold, dense air masses spreading out along the surface. Concurrent soundings of the lower atmosphere suggest the sources of cold pools are downdrafts originating from above the boundary layer cooled by evaporation in the lower midtroposphere, consistent with models (Skylvingstad and de Szoeke 2015) and previous observations of deep convective cold pools over tropical oceans [Zipser (1977); GATE (Barnes and Garstang 1982; Johnson and Nicholls 1983); COARE (Young et al. 1995; Saxen and Rutledge 1998); and Rain in Cumulus over the Ocean (RICO; Zuidema et al. 2012)].

The frequency and strength of cold pools are strongly related to the phase of intraseasonal MJO events (de Szoeke et al. 2015). Cold pools modulate intraseasonal surface air temperature variability by cooling the surface air while SST is still warm in the onset phase of the MJO. Dropsondes released from aircraft in DYNAMO have shown deeper and stronger cold pools, which recover more

slowly, in the convectively suppressed phase of the MJO, when air in low to midlevels is drier (Chen et al. 2016).

Cold pools have several direct effects on the surface and atmospheric BL meteorology. Wind speed and ocean–atmosphere surface temperature difference anomalies affect surface fluxes (e.g., Barnes and Garstang 1982; Young et al. 1995; Jabouille et al. 1996; Saxen and Rutledge 1998). In the southern intertropical convergence zone in DYNAMO, cold pools increased wind in the same direction as the mean wind, enhancing the surface fluxes (Yokoi et al. 2014). Though the wind stress magnitude increased as a result of the cold pools, surface latent heat flux decreased in more convectively active LESs forced with greater moisture convergence (Skylvingstad and de Szoeke 2015) because of the increased surface air humidity.

A further aspect of the boundary layer thermodynamic budget on which consensus has not yet been achieved is the relative contribution of different sources for moisture and moist static energy to subsequent convection. Despite agreement that anomalous moisture [or moist static energy (MSE)] is a prerequisite for convection, whether its origin is rain evaporation, surface fluxes, or preexisting moisture anomalies from, say, previous cold pools, remains a matter of debate (Tompkins 2001; Li et al. 2014; Langhans and Romps 2015; Torri and Kuang 2016; Schlemmer and Hohenegger 2016). The moisture sources also interact with the convective dynamics. Here also basic observations provide useful metrics against which to gauge model behavior.

Using surface time series, soundings, and remote sensing observations from DYNAMO, this study addresses 1) the structure of cold pools, 2) the effect of intraseasonal atmospheric variability on the frequency and strength of cold pools, and 3) the contribution of cold pools, surface fluxes, and entrainment to BL air properties. The remainder of this paper is organized in sections as follows. Section 2 gives an overview of cold pools observed in DYNAMO, the methods used to identify them from time series, their vertical structure from soundings, and their influence on air properties of the BL. Section 3 presents the relationship between cold pool statistics in convective versus suppressed phases of the MJO. Section 4 presents cold pool structure, fluxes, and recoveries; a diagnosis of hydrostatic pressure gradients due to cold pools; and their relation to rain showers. Section 5 presents a summary.

2. Cold pools observed in DYNAMO

a. Time series

SST variability observed on the *Revelle* during the DYNAMO field campaign while on station at 0°, 80°E is

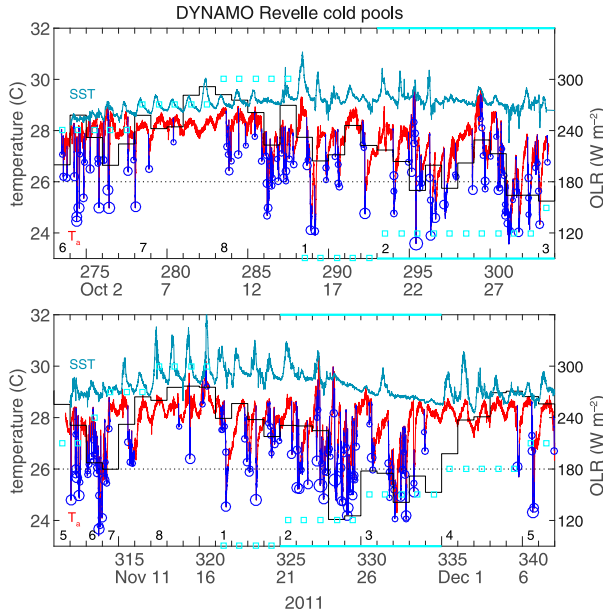


FIG. 1. Time series of surface air (red) and ocean (sea blue) temperature for the R/V *Revelle* legs 2 and 3 in DYNAMO. Cold pool temperature drops and recoveries are blue. The size of the circle on the minimum temperature in each cold pool indicates the strength of the cold pool. Daily NOAA interpolated OLR is indicated by the thin black line. The RMM phase (1–8) is indicated by cyan squares and digits along the bottom axis.

dominated by two intraseasonal humps: one in leg 2 (30 September–30 October 2011) and one in leg 3 [7 November–7 December 2011; Fig. 1 (de Szoeke et al. 2015)]. Air temperature T has relatively weak intraseasonal variability and is instead punctuated by “cold pools” that exhibit a quick drop, followed by a gradual recovery. The compressed time scale of Fig. 1 emphasizes the strongest and longest-lasting cold pools, some of which take about 1 day to recover completely. Figure 2 shows the cumulative probability distributions and probability densities for surface air temperature, wet-bulb temperature, and sea surface temperature (SST). Air temperature has a strong negative tail as a result of the cold pools, while wet-bulb temperature is only slightly negatively skewed. SST is positively skewed because of solar diurnal warming during calm periods (Matthews et al. 2014). The relationship of the cold pools to convective activity and their effect on daily to intraseasonal temperature variability will be explored in section 3.

Cold pool fronts are identified by the unfiltered 1-min-mean surface temperature measured by the NOAA/ESRL/Physical Sciences Division (PSD) aspirated thermometer on the forward mast of the R/V *Roger Revelle*. The identification algorithm is designed to be sensitive to asymmetric cooling events visible in the time

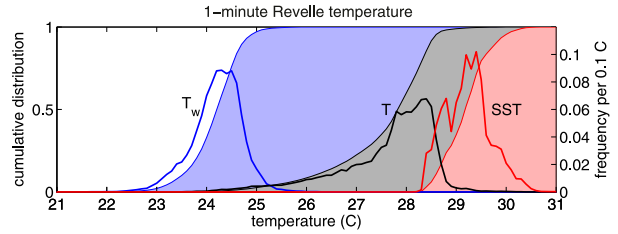


FIG. 2. Cumulative and probability density diagrams for surface air wet-bulb temperature T_w (blue), temperature T (black), and sea surface temperature (red).

series yet insensitive to high-frequency noise, to exclude false positives, and to group coincident fronts as one single event. It is efficient to implement in a few simple steps on a computer. First, the temperature time series is smoothed with a running 11-min centered triangular window. A series of simple thresholding operations are then applied to the smoothed time series to identify cold pools: 1) Cold pool candidate temperature minima are identified where the temperature is the minimum of the previous 20-min window. To avoid multiply identifying a single cold pool, 2) contiguous (separated by 1 min) minima are combined, and 3) minima within 20 min of each other are combined if the temperature does not exceed either minimum by 0.5°C . 4) The low-pass temperature drop δT is computed as the difference between the maximum T within 20 min of the first T minimum in the event and the last T minimum in the event. 5) Temperature drops δT are retained that exceed a 0.7°C threshold. 6) The minimum unfiltered temperature T_{\min} (at time t_{\min}) associated with this temperature drop and maximum temperature T_{\max} (at time t_{\max} within 40 min of T_{\min}) are identified. This (stronger) refined temperature drop is called $\Delta T \equiv T_{\max} - T_{\min} = T(t_{\max}) - T(t_{\min})$.

Low-pass temperature drops have a long-tailed distribution which decrease as $\delta T^{-1.67}$ for $0.07 < \delta T < 0.7$ and more steeply ($\delta T^{-2.67}$) for $\delta T > 0.7^\circ\text{C}$. The 215 cold pools selected by the threshold of 0.7°C indicated on the temperature time series (Fig. 1) are the strongest 14% of the temperature drops δT .

The lowest temperature minima T_{\min} have the strongest temperature drops ΔT (Fig. 3). A practical limit for ΔT is $\Delta T \leq 30^\circ\text{C} - T_{\min}$ (green line, Fig. 3). Several cold pool fronts with relatively weak ΔT can combine to significantly lower the air temperature. We diagnose the recovery time τ of a cold pool as the time elapsed when the low-pass temperature first rises by $\Delta T/e$ above its minimum. Recovery time scales will be compared with estimates of the depth of the cold pools and surface fluxes within the recovery in section 4c.

Rain was observed by the *Revelle* optical rain gauge within ± 20 min of the cold pool front for 141 cases

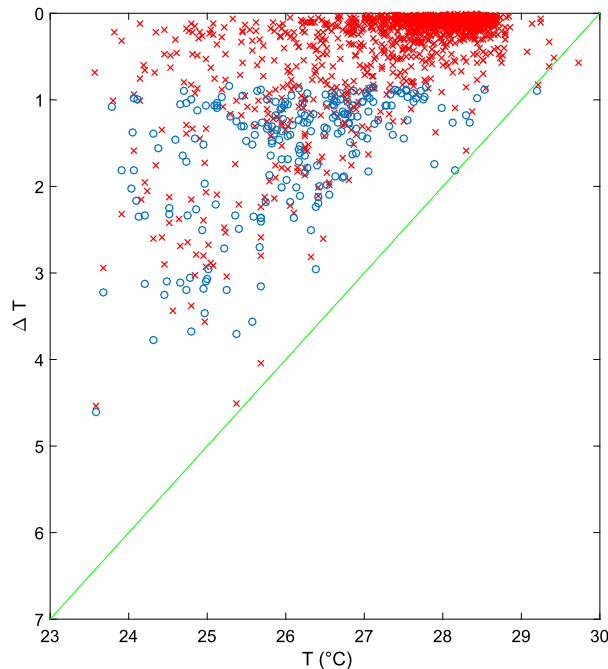


FIG. 3. Cold pool temperature drop ΔT vs T_{\min} at the cold pool wake onset. Red crosses show 1501 distinct events where the 6-min low-pass T is the lowest of the previous 20 min. Blue circles show 215 events where temperature drops by more than 0.7°C ; their minimum and maximum T are estimated from the unfiltered time series.

(65%). We refer to this subset as “rainy” cold pools. As shown in Fig. 4, the relationship of the cold pool onset to the parent convection does not become clear until a temperature drop of approximately 1.5 K, at which value the cold pool onset becomes more clearly associated with rain after the initial temperature drop. Some of the rain events are isolated, short-lived showers, while others are longer-lived events that continue for at least 1.5 h after the initial temperature drop.

The high-resolution temporal variability of the cold pools in the 1-min time series is not observed by the 3-hourly soundings. Thus, we identify “cold pool”

soundings (to be shown later in Figs. 8 and 9) as those with air surface temperatures below 26.5°C (the 10th percentile of the air temperature distribution; Fig. 2). “Undisturbed” soundings have surface temperature exceeding 27.5°C (40th percentile). Temperature thresholding works well for the soundings because there is very little other temperature variability besides cold pools.

b. Temporal structure

The unfiltered 1-min-average NOAA/ESRL/PSD air temperature time series is used for cold pool identification as above. We additionally use the DYNAMO data distributed by the University of Connecticut [Edson et al. (2016), described in de Szoeke et al. (2015)], which combines multiple measurements into a consistent synchronized time series. Of the 215 cold pools identified from the PSD surface temperature time series, 211 coincide with the University of Connecticut time series. Figure 5 shows the composite-mean temporal structure of surface air and ocean temperature, specific humidity, and wind speed for all the cold pools, 1 h before the time t_{\max} of the temperature maximum to 1 h after the time t_{\min} of the temperature minimum. Between the temperature maximum and minimum, a normalized time coordinate resolves the evolution of variables in the cold pool front with 20 points. The median time elapsed between the temperature maximum and minimum was 21 min. We refer to the time period between t_{\max} and t_{\min} as the “front.” This front-relative time coordinate is used for compositing fluxes, rain rate, and water vapor and liquid water paths. Figure 6a shows the distribution of the duration of cold pool fronts and the distance traveled along the path of wind.

The mean air temperature drop across the front is 1.3°C (Fig. 5c). About half of this cooling recovers within the hour after the front. After falling by 0.6 g kg^{-1} in the front, specific humidity recovers more quickly than air temperature. Mean wind speed increases more than 25% during passage of the front and stays $\sim 0.4\text{ m s}^{-1}$ stronger throughout the hour following the front. Mean SST decreases

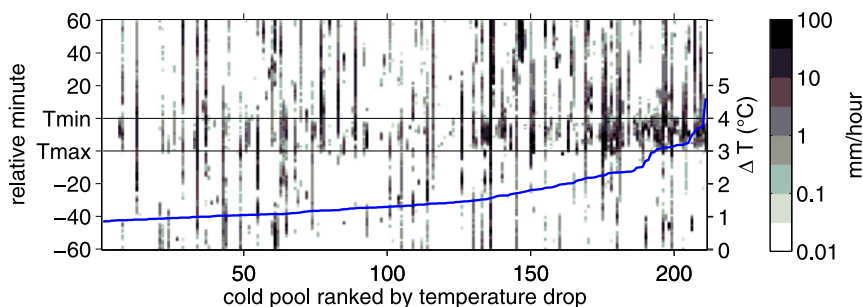


FIG. 4. Rain time series within ± 1 h of the cold pool front ranked according to ΔT (blue line).

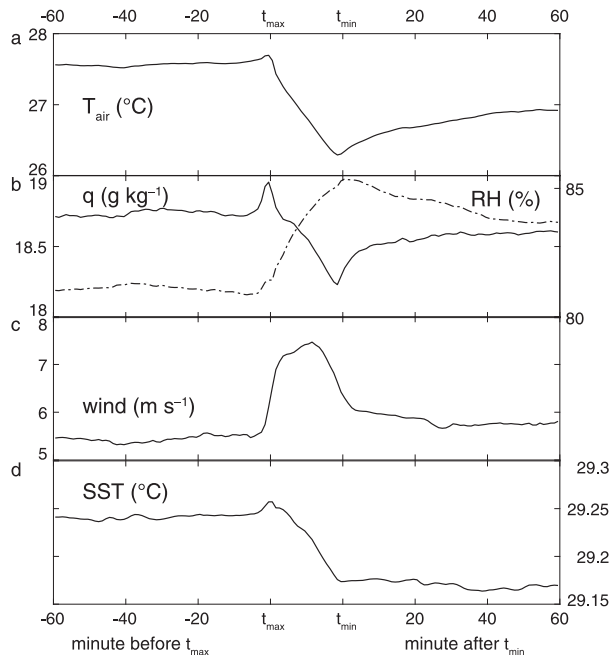


FIG. 5. Mean (a) 10-m air temperature, (b) specific and relative humidity, (c) wind speed, and (d) SST composited on time elapsed from the start (t_{\max}) and end (t_{\min}) of the cold pool front and on a normalized time coordinate between t_{\max} and t_{\min} .

continuously, with a sharp drop of 0.08°C as the front passes, followed by a slight cooling in the hour following the front (Fig. 5d). Persistent SST cooling is likely due to increased surface heat fluxes and subsurface entrainment.

Slight increases in the specific humidity (0.25 g kg^{-1}), temperature (0.1 K), and even SST (0.01 K) are evident before the front at t_{\max} . We cannot rule out the possibility that the specific humidity rises at t_{\max} just because of compositing on the temperature maximum. The magnitude of the mean specific humidity peak corresponds to the increase of the saturation specific humidity due to the temperature peak. Relative humidity responds inversely to air temperature, with a minimum 3 min before the peak of specific humidity. In any case, appearance of the specific humidity peak coinciding with an increase in temperature before the front argues against a direct connection to rain evaporation from the parent convection. If it is not a compositing artifact, plausible origins of the moisture anomaly could be surface flux or convergence of preexisting warm moist anomalies by the encroaching wind gust, perhaps before turbulence entrains drier air from above.

Figure 7 shows the time series of air temperature, specific humidity, and wind speed for each of the 211 cold pools, sorted by each cold pool's air temperature drop ΔT . Figures 7a and 7b also show ΔT by which the cold pools were sorted and the specific humidity change

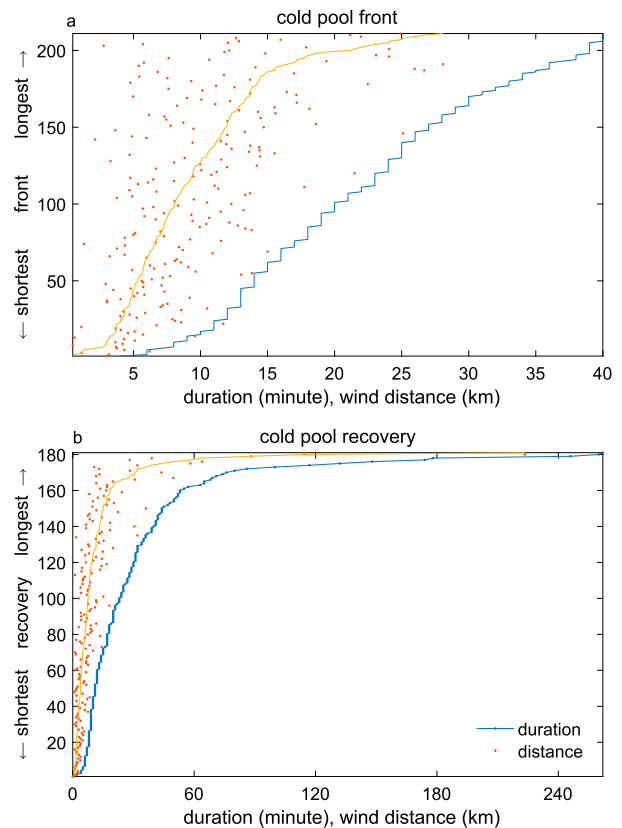


FIG. 6. Sorted time duration (blue) and wind path distance (yellow) during cold pool (a) fronts and (b) $1/e$ temperature recoveries. Red points show path distances sorted by event duration.

over the front. Stronger cold pools have stronger humidity decreases (up to about 2 g kg^{-1}) than the mean. Humidity change variations of $\sim 1\text{ g kg}^{-1}$ unrelated to the strength of ΔT are common. The maximum 1-min-mean wind speed within the front, compared to the wind speed at the time of the temperature maximum at the onset of the front, increases for stronger cold pools, but with considerable variability among events regardless of the strength of the temperature drop. Sea surface temperature decreases by 0.1°C in the mean. A few of the stronger cold pools have strong SST decreases of 0.8°C that continue to cool for an hour following the front. The changes in these variables affect the surface fluxes, as will be shown in section 4a.

c. Vertical structure

Figure 8 shows the time–height series of wet-bulb potential temperature θ_w from radiosondes released from the R/V *Revelle* during legs 2 and 3 of DYNAMO. Deep low- θ_w (dry) layers are evidence of large scale variability in the midtroposphere. Wet-bulb

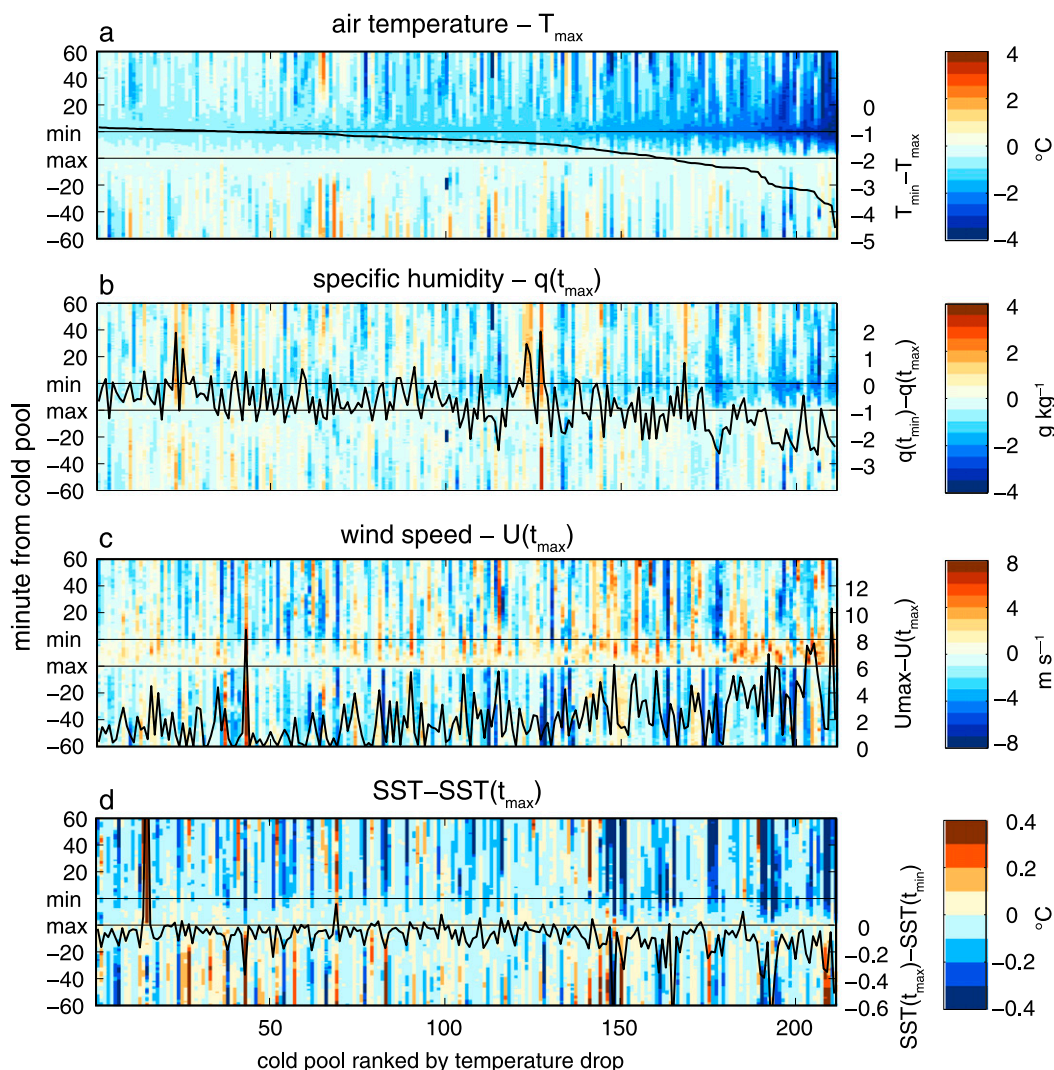


FIG. 7. Time series for ± 1 h from the cold pool front, ordered by the strength of the diagnosed temperature drop ΔT . (a) Temperature relative to the maximum temperature; (b) specific humidity relative to specific humidity at t_{\max} ; (c) wind speed relative to wind speed at t_{\max} ; and (d) SST relative to the SST at t_{\max} .

temperature measured at about 20-m altitude from the ship's forward mast is overlaid on Fig. 8. For 20–30 of the longer-lasting drops in surface T_w , θ_w decreases in the BL but increases aloft (800–400 hPa), reflecting a shift to a moister, more well-mixed profile in deep convective events.¹ There are 20 consecutive sounding pairs in DYNAMO legs 2 and 3 where 0–500-m θ_w decreases by at least 1°C. In many cases, the 1-min

¹ While the potential temperature is nearly moist adiabatic above the BL, the environment is far from saturated. Narrow cloudy updrafts (and evaporating downdrafts) set the temperature profile to a moist adiabat, yet moisture rains out and is detrained, leaving the environment unsaturated.

surface temperature drops even more rapidly between the times of the soundings.

Surface temperature T and surface wet-bulb temperature T_w both are observed to drop abruptly at the start of cold pools. Evaporation of cloud or rain liquid in an otherwise adiabatic process conserves θ_w . Thus, downdrafts that introduce lower θ_w from aloft explain the decrease of surface T_w . Surface temperature T drops even more than T_w because, while it conserves θ_w , evaporation of rain in the BL further cools θ . Because of evaporation, a saturated downdraft will have higher q_v than the lower midtroposphere parcel from which it originates, yet, because of its temperature, a cold pool usually has lower specific humidity q_v than the warm surface air it displaces (Fig. 7b).

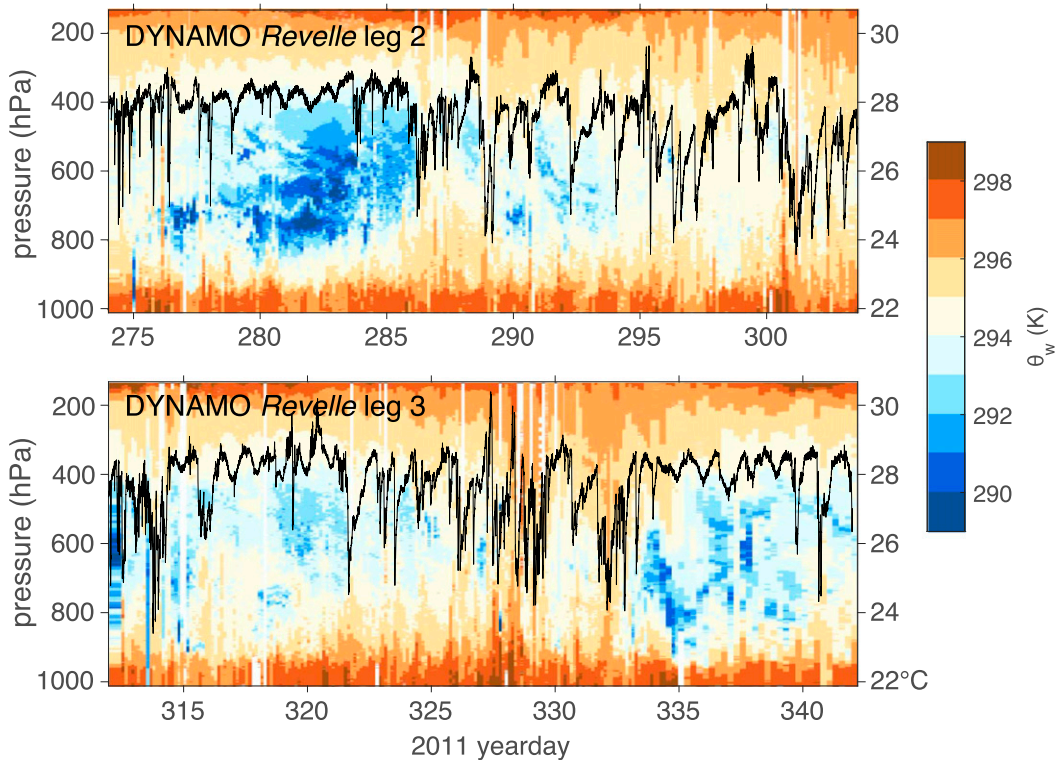


FIG. 8. Wet-bulb potential temperature θ_w from soundings (shaded) and wet-bulb temperature (black) for DYNAMO *Revelle* legs (top) 2 and (bottom) 3. Soundings are 3 hourly for yeardays 275–333 (2 Oct–29 Nov 2011), excluding the port call. Starting yearday 334, they are 6 hourly.

Profiles of conserved variables potential temperature θ , wet-bulb potential temperature θ_w , and specific humidity q_v indicate the depth of cold pools and the degree to which the cold pool temperature has recovered at the point that the sounding encounters it. Equivalent potential temperature θ_e and wet-bulb potential temperature θ_w are both conserved in adiabatic and saturated pseudoadiabatic processes. We use θ_w because of its correspondence with surface properties.

Figure 9 shows a 2.5-day (0600 UTC 29 October–1200 UTC 30 October 2011) time series of surface temperature and wet-bulb temperature. Three cold pools are evident in the time series as rapid cooling events on 28, 29, and 30 October. The nearest soundings were chosen before and after the cold pool front. Profiles of the lowest 1.5-km potential temperature and wet-bulb potential temperature compare air in the cold pool (blue) to the undisturbed air before the front (red). In each case, the potential temperature after the cold pool front is colder than before the front by ~ 2 K at the surface, but with very little change in θ at 700–800 m. The potential temperature of the air in advance of the cold pool is nearly constant below 500 m but decreases downward for the cold pool soundings. Surface mixed layers, with nearly uniform

potential temperature, are shallower for the cold pool soundings. In the first two cold pool soundings, θ_w is more uniform and lacks the higher- θ_w layer in the lower 500 m that characterizes the air before the cold pool. The sounding before the third cold pool may itself be under the immediate influence of a weak cold pool. Though the difference in θ is clear, the difference in θ_w is negligible below 300 m, suggesting rain evaporation in the subsaturated BL conserves moist static energy.

Figure 10 shows the average profiles of θ and θ_w for “cold” soundings with 10-m sounding temperature $T < 26.5^\circ\text{C}$ (blue) and “warm” soundings with $T > 27.5^\circ\text{C}$ (red). The soundings in each category are plotted as tiny dots to illustrate the distribution of the profiles. Above 800 m, the difference between the warm and the cold composite potential temperature soundings is 0.4–0.8 K, and the mean difference increases nearly linearly downward from 800 m, to 2.8°C at the surface. Cold soundings follow a moist adiabat (with constant θ_w) nearly all the way to the surface, while the warm soundings have constant potential temperature in the BL. Thus, we suspect the dominant source of surface cooling is moist adiabatic evaporation of cloud and rainwater in the BL.

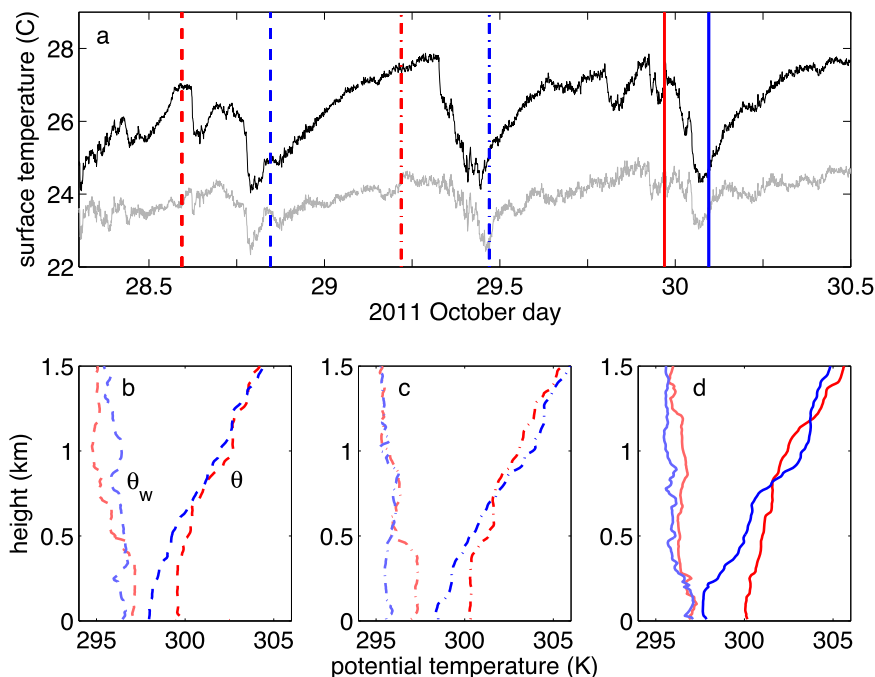


FIG. 9. (a) The 2.5-day time series of potential temperature θ (black) and wet-bulb potential temperature θ_w (gray). (b)–(d) Soundings of the lower 1.5 km in undisturbed conditions before the cold pool (red) and in the cold pool wake (blue). The corresponding times of the soundings are indicated by like vertical lines in (a).

This is corroborated by θ_w , which, for warm soundings, is relatively warm (297.3 K) in a 500–800-m BL, and has a weak negative gradient of θ_w to about 2.7 km. Wet-bulb potential temperature is nearly the same for the cold soundings as for the warm soundings above 1.5 km, but the difference grows downward. Presumably, air in the cold soundings originated as air with lower θ_w above the BL and descended to the surface, conserving θ_w .

d. Conserved-variable analysis of boundary layer air

We use conserved variables potential temperature θ and water vapor specific humidity q to characterize the sources of BL air and their variability. Potential temperature is conserved within the BL as long as there is no condensation or evaporation. Saturated downdrafts, indicated by subscript d , inject relatively cold dry air at (θ_d, q_d) into the BL. Flux from the saturated sea surface warms and moistens the BL toward (θ_0, q_0) . Entrainment brings warm dry air at $(\theta_{\text{entr}}, q_{\text{entr}})$ into the BL from the cumulus inversion layer at 800 m.

The ~ 15 -m ship measurement height is assumed to be within a surface layer with constant flux and strong gradients. We estimate properties (θ_b, q_b) of the mixed boundary layer outside the surface gradient layer by adjusting the 15-m observations to a height (100 m) outside the surface layer using Monin–Obukhov

flux–gradient similarity theory (e.g., de Szoeke et al. 2012). This only accounts for gradients associated with the surface layer. The adjustment is insensitive to the choice of the nominal height as long as it is outside the surface layer. The effect of this flux–gradient transformation is to cool θ by ~ 0.1 K and dry q by ~ 0.5 g kg $^{-1}$ relative to the surface. The sea surface potential temperature and saturation mixing ratio (θ_0, q_0) is computed from the skin temperature from a thermistor floating at 0.1 m. The effects of the molecular skin layer are modeled (Fairall et al. 1996). The $(\theta_{\text{entr}}, q_{\text{entr}})$ of entrained air is interpolated from soundings at 800 m, where there is an inflection point in the mean potential temperature and humidity profiles. The downdraft (θ_d, q_d) is taken to be the wet-bulb potential temperature θ_w of the soundings averaged from 2.5 to 3.5 km, where θ_w is nearly uniform with height.

Though there are anecdotes of undiluted downdrafts descending from ~ 3 km, most studies show that properties of downdrafts are more representative of air at 1–2 km (e.g., Zipser 1969; Betts 1976; Zipser 1977; Kingsmill and Houze 1999; Torri and Kuang 2016). Because wet-bulb potential temperature is nearly uniform with height throughout the free troposphere, our results are not very sensitive to the choice of origin. Conversely, because of the uniformity of θ_w , we cannot independently determine the origin height of the

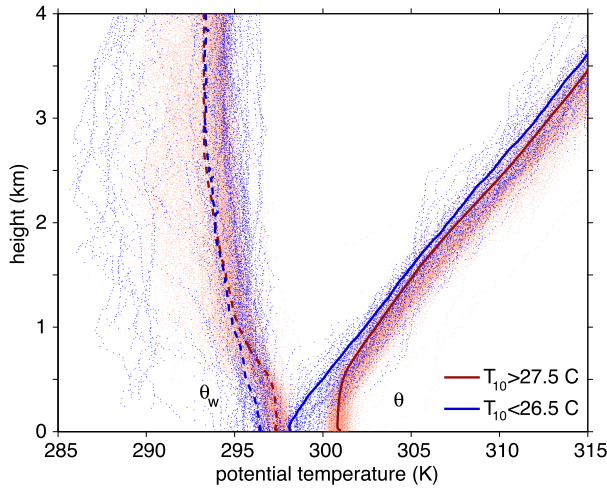


FIG. 10. Rawinsonde profiles of potential temperature θ and wet-bulb potential temperature θ_w . Sondes colored blue meet a simplified cold pool criterion: $T_{10m} < 26.5^\circ\text{C}$. Sondes colored red meet a simplified undisturbed criterion: $T_{10m} > 27.5^\circ\text{C}$.

downdrafts. We choose to use θ_w from 2.5 to 3.5 km, which is $\sim 1\text{ K}$ lower than at 1–2 km. This choice compensates somewhat for the overestimate of downdraft θ_w by the soundings, which mostly sample the environment and not the downdrafts. Mixtures including downdrafts assumed to have θ_w representative of 1–2 km can explain most of the BL observations but do not explain a significant number of the coldest driest cases. Using the cooler θ_w from 2.5–3.5 km for the downdrafts explains all but 2% of the coldest driest BL observations.

Figure 11a shows the BL observations surrounded by downdraft, surface, and entrainment end members. The inversion air at 800 m has nearly the same specific humidity as the saturated downdrafts and nearly the same potential temperature as the saturated sea surface. Including unsaturated inversion air in the mixture is essential to explain the unsaturated BL air. Of the BL observations, 98% can be explained as mixtures among the saturated surface, the saturated downdraft, and the entrained 800-m air. The remaining 2% of BL observations are unusually cold and dry (Fig. 11a). These BL observations cannot be explained by mixtures, probably because the 3-hourly soundings undersample infrequent and short-lived downdrafts responsible for cooling and drying the surface air.

We have assumed that downdrafts originate from above the BL and remain saturated by evaporation of rain as they descend to the top of the BL (yellow circles in Fig. 11a). To test the possibility that the BL is cooled in situ by evaporation of rain falling into it, we compute the wet-bulb potential temperature and its corresponding saturation specific humidity from the soundings within the BL. The potential temperature and humidity that

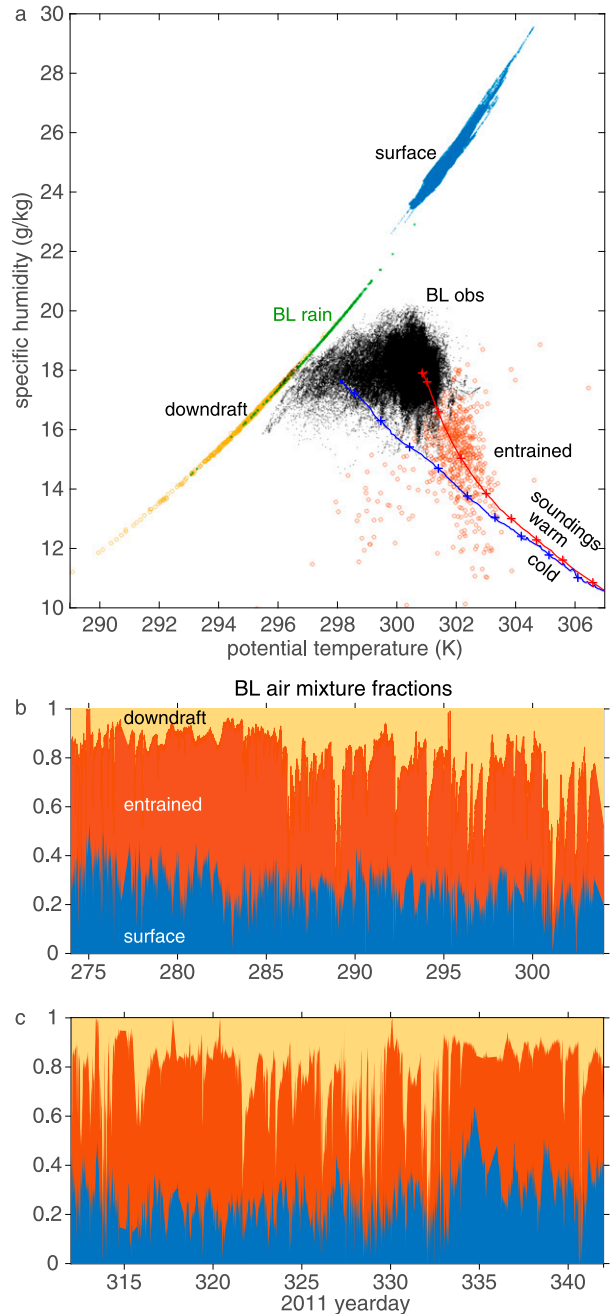


FIG. 11. (a) Air observed in the boundary layer (black) on conserved potential temperature and specific humidity coordinates along with the properties of three end members: saturated downdrafts (yellow circles), the saturated sea surface (blue points), and the stratified cumulus layer above the BL (orange circles). Two percent of the observations, mostly that are drier than the interpolated sounding, cannot be represented by a mixture of these end members. Green points represent the wet-bulb temperature that would be reached by evaporation of rain in the BL. Red and blue lines are the mean soundings from Fig. 10, with crosses marking every 200 m. (b),(c) Mixture fractions of saturated downdraft, air in equilibrium with the sea surface, and air entrained from the cumulus layer.

would be reached by saturating the BL by evaporation at 200–300 m (green points in Fig. 9a) is warmer and moister than the downdrafts and not cold and dry enough to explain 8% of the surface temperature and humidity observations. Since only 10% of surface air temperatures are lower than 26.5°C, most of the air identified with cold pools cannot be explained by rain evaporation in the BL. We conclude that, rather than evaporatively cooled BL air, saturated downdrafts with wet-bulb potential temperature representative of air well above the BL are responsible for the coldest air observed at the surface.

Properties of boundary layer air cluster in linear rays that point to the moist properties of the sea surface end member. These linear clusters are most evident on the dry side of the q - θ distribution (black points, Fig. 11a). Time animations of the points in Fig. 11 show potential temperature increases quickly (moving to the right on Fig. 11a), approaching the sea surface and entrained BL-top potential temperature. BL specific humidity recovers more slowly (upward). Air is continually kept drier than the sea surface saturation humidity q_0 by entrainment that is not directly related to cold pools (Figs. 11b,c). In the long term, potential temperature recovers toward the properties of entrained air, with 71% of BL potential temperature observations above 300 K. Downdrafts are instrumental in keeping the BL cooler than both the sea surface and air entrained from above the BL.

Writing the BL temperature and specific humidity (θ_b , q_b) as a mixture of f_0 parts air in equilibrium with the saturated sea surface, f_d parts saturated downdrafts, and f_{entr} parts air entrained from the inversion,

$$\theta_b = f_0\theta_0 + f_d\theta_d + f_{\text{entr}}\theta_{\text{entr}}, \quad (1)$$

$$q_b = f_0q_0 + f_dq_d + f_{\text{entr}}q_{\text{entr}}, \quad \text{and} \quad (2)$$

$$f_0 + f_d + f_{\text{entr}} = 1. \quad (3)$$

Equations (1)–(3) are solved simultaneously for the three mixing fractions (f_0 , f_d , and f_{entr}) from the known BL mixture (θ_b , q_b) and its three known end members. Figures 11b and 11c show the time series of f_d , f_{entr} , and f_0 . The mean BL air mixture is 51% entrainment, 22% downdrafts, and 27% in equilibrium with the sea surface. Bursts of high downdraft fractions f_d indicate times when undiluted downdraft air was recently injected into the BL.²

²The mixing fractions can be considered nondimensional transfer velocities $f_i = W_i/W_{\text{tot}}$ so that they describe the relative role of different fluxes into a mixed layer where heat balance is $W_d(\theta_d - \theta_{\text{BL}}) + W_0(\theta_0 - \theta_{\text{BL}}) + W_{\text{entr}}(\theta_{\text{entr}} - \theta_{\text{BL}}) = 0$ with $W_d + W_0 + W_{\text{entr}} = W_{\text{tot}}$.

Does radiative heating of the boundary layer affect the mixing fractions? The effect of radiative heating is added to (1) as

$$\theta_b = f_0(\theta_0 + r) + f_d\theta_d + f_{\text{entr}}\theta_{\text{entr}}, \quad (4)$$

where $r = [\rho c_p(\theta_0 - \theta_b)/H][F_{\text{rad}}(z_i) - F_{\text{rad}}(0)]$. The first quantity in square brackets scales the radiative flux difference to the known surface sensible heat flux H . We diurnally average the 0–500-m radiative heating from the Addu Atoll combined radar retrieval [CombRet; Z. Feng 2016, personal communication; after Feng et al. (2014), but using surface temperature representative of SST] in 3-h intervals and apply it to the appropriate local time at the *Revelle*. Average heating rates are about -1 K day^{-1} , with a diurnal cycle from $+1 \text{ K day}^{-1}$ in daylight to -2 K day^{-1} at night. This diurnally repeating heating rate over the $z_i = 500$ -m mixed layer does not have a significant effect on the mixing fractions. Radiation increases the average surface mixing fraction f_0 by $+0.013$ at the expense of f_d and f_{entr} .

3. Intraseasonal synoptic variability and cold pools

On the equator during DYNAMO, convectively active conditions are associated with the MJO and equatorial Kelvin waves (Yoneyama et al. 2013; Moum et al. 2014). We use the phase of the global Realtime Multivariate MJO (RMM) index (Wheeler and Hendon 2004) to categorize the ship observations in the context of the MJO. We describe MJO at 80°E as convectively *active* for RMM phases 2–3, convectively *disturbed* preceding this in RMM phase 1, and convectively *suppressed* in all other RMM phases (4–8). Because local conditions are better correlated to local convection (de Szoeke et al. 2015), we also use satellite $1^\circ \times 1^\circ$ average daily NOAA interpolated outgoing longwave radiation (OLR; Lee 2014) at the grid centered over the ship to indicate convective conditions (Fig. 1, thin black stepped line). Low OLR indicates high clouds and deep convective activity, while high OLR indicates relatively shallow clouds and/or clear skies.

The statistics of cold pools observed at the *Revelle* are correlated with the phase of the MJO, indicated by the phase of the RMM index (cyan in Fig. 1). Cold pools are more common during convectively active conditions of the MJO. The frequency of cold pools doubles in the active phase (4.9 day^{-1}) compared to the suppressed phases (2.5 day^{-1} ; Table 1). The amount of time the ship spent in cold pools (i.e., between t_{max} and the recovery time) more than doubles from the suppressed phase (1.8 h day^{-1}) to the active phase (4.3 h day^{-1}). Along with the greater temporal influence of cold pools, the

TABLE 1. Intraseasonal composite-average air temperature T , specific humidity q , number of cold pools per day N_{cp} , average time spent in cold pools T_{cp} , and fractions of downdraft f_d , entrained f_{entr} , and surface f_0 air for convectively suppressed (RMM phases 4–8), disturbed (RMM phase 1), and active (RMM phases 2 and 3) days, and all days of DYNAMO *Revelle* legs 2 and 3.

Intraseasonal phase	T (°C)	q (g kg ⁻¹)	N_{cp} (day ⁻¹)	T_{cp} (h day ⁻¹)	f_d	f_{entr}	f_0
Suppressed (4–8)	27.94	17.34	2.5	1.8	0.17	0.54	0.29
Disturbed (1)	27.57	17.56	3.2	3.0	0.25	0.50	0.25
Active (2 and 3)	27.23	17.74	4.9	4.3	0.30	0.45	0.25
All	27.66	17.52	3.6	2.9	0.22	0.51	0.27

fraction of downdraft air observed at the ship increases from 0.17 in the suppressed phase to 0.30 in the active phase, and entrainment into the BL decreases more than surface fluxes to accommodate the greater fraction of downdraft air (Figs. 11b,c). The influence of surface flux on the BL air is relatively greater in the suppressed phase than in the active or disturbed phases. Downdrafts and entrained air from the cumulus inversion layer have similar humidity in the suppressed (15 g kg⁻¹) and disturbed (15.5 g kg⁻¹) phase. In the active phase, higher downdraft wet-bulb potential temperature and saturation specific humidity (16 g kg⁻¹) increases the BL humidity slightly.

The daily surface temperature is significantly anti-correlated ($r = -0.62$) with the frequency of cold pools, with an empirical sensitivity of the daily surface $\langle T_{sfc} \rangle$ temperature given by

$$\langle T_{sfc} \rangle = 28.08^\circ\text{C} - (0.12^\circ\text{C})\langle F_{CP} \rangle,$$

where $\langle F_{CP} \rangle$ is the frequency of cold pools per day. On average, each cold pool reduces the daily temperature by about 0.1°C, 19% of the daily average standard deviation. Because of their skewed temperature and duration distribution, cold pools that are much colder and longer lasting than the average are disproportionately responsible for the average cooling.

Cold pools are more frequent on days with lower OLR (Fig. 12c; $r = -0.49$; only significant correlations at 0.95 confidence are shown). Daily surface temperature is positively correlated ($r = +0.64$) with OLR (Fig. 12a). The cumulative count of cold pools against the daily OLR shows a steady distribution of cold pools over the range of OLR (Fig. 10d). Daily OLR fell in the ranges 170–180 W m⁻² for 6 days and 230–240 W m⁻² for 11 days, explaining why more cold pools were detected in these ranges. The lowest quartile of days with OLR < 198 W m⁻² has 82 (38%) of the cold pools detected, while the top quartile (OLR > 260 W m⁻²) has only 30 (14%) of the cold pools.

Cold pools are less frequent when OLR is higher. Chen et al. (2016) found strong cold pools beneath dry-air anomalies associated with the convectively

suppressed phase of the MJO. We find that the average strength of the cold pools is not correlated to the large-scale convective activity, though some of the strongest cold pools do occur in more suppressed conditions (Fig. 12b). The profile of potential temperature varies little with time (Fig. 10). The strongest θ_w anomalies are negative (Fig. 8), because of dry anomalies in the lower midtroposphere advected from drier regions (Chen et al. 1996; Kerns and Chen 2014). Descent of dry air alone cannot explain the dry anomaly because radiative cooling is insufficient to balance the implied adiabatic warming (Mapes and Zuidema 1996).

4. Composite cold pools

a. Evolution of surface fluxes

Wind gusts and cold air temperature in cold pools affect the turbulent surface fluxes through their wind speed, surface ocean–air temperature difference, and specific humidity difference. Figure 13b shows the evolution of the composite-mean surface wind stress magnitude and sensible and latent heat flux over the more than 2 h surrounding the cold pool frontal passage for the 211 cold pools.

Surface fluxes and u^* , T^* , and q^* are computed from the 1-min data with the COARE 3.5 bulk aerodynamic flux algorithm with the wind speed gust enhancement disabled, assuming the 1-min observations already resolve wind gusts. We factor the stress and sensible and latent heat fluxes as products of the friction velocity u^* and surface turbulent temperature scale T^* and specific humidity scale q^* :

$$\begin{aligned} \tau &= \rho u^{*2}, \\ H &= \rho c_p u^* T^*, \quad \text{and} \\ E &= \rho L u^* q^*, \end{aligned}$$

where ρ and c_p are the density and specific heat of air and L is the latent heat of vaporization of water. The heat fluxes over the 211 cold pools are decomposed as the dominant products of composite mean $\langle u^* \rangle$, $\langle T^* \rangle$, and $\langle q^* \rangle$, and the interevent covariance of anomalies:

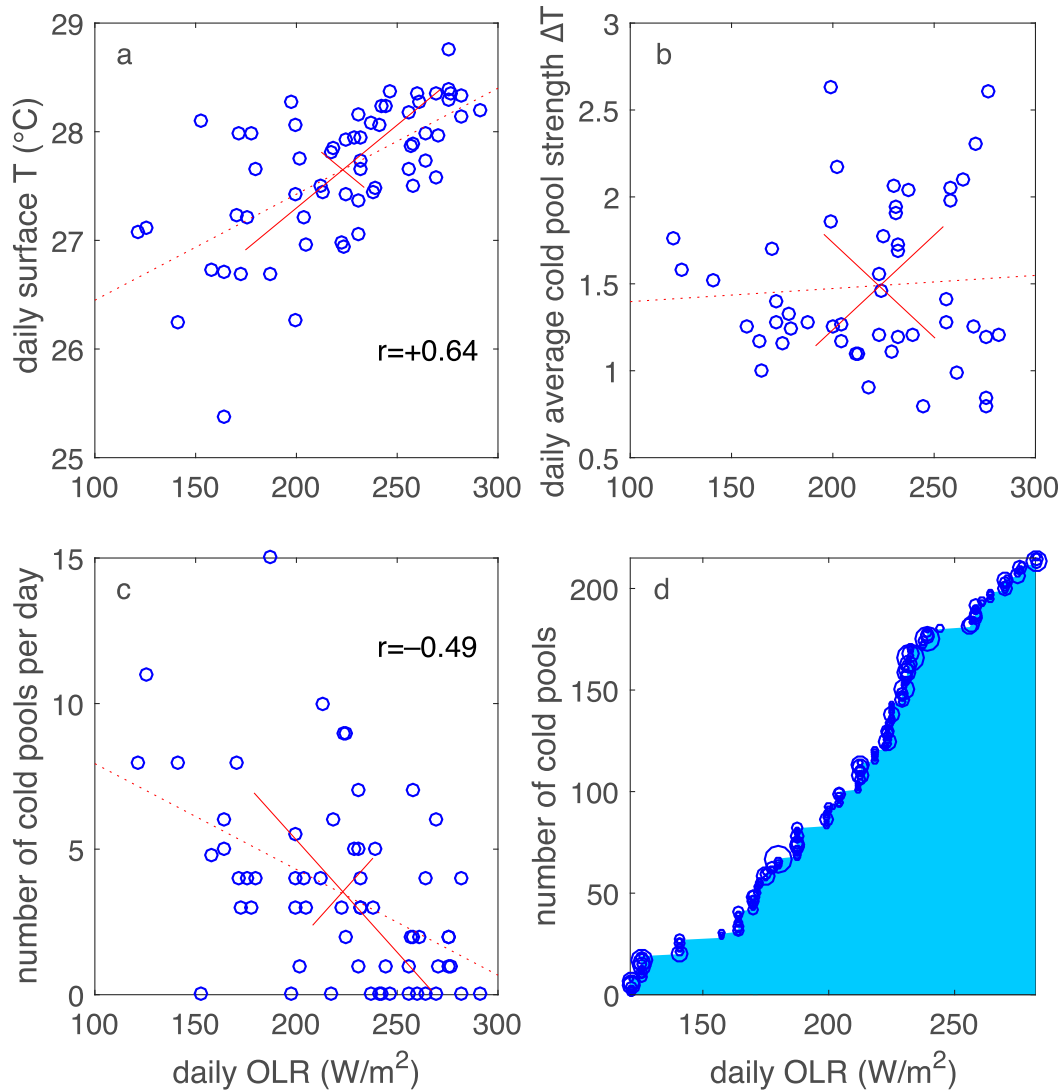


FIG. 12. (a) Daily surface temperature as a function of OLR. (b) Average cold pool strength as a function of daily OLR. (c) Daily frequency of cold pools vs OLR. (d) Cumulative distribution of cold pools vs OLR. The red cross shows the dimensional major and minor eigenvectors of the standardized covariance matrix; the red dashed line is the regression line.

$$\begin{aligned}\langle u^{*2} \rangle &= \langle u^* \rangle^2 + \langle u^{*l2} \rangle, \\ \langle u^* T^* \rangle &= \langle u^* \rangle \langle T^* \rangle + \langle u^{*l} T^{*l} \rangle, \quad \text{and} \\ \langle u^* q^* \rangle &= \langle u^* \rangle \langle q^* \rangle + \langle u^{*l} q^{*l} \rangle.\end{aligned}$$

We use average density ρ and latent heat L to get fluxes from this decomposition. The density ρ changes about 2%, and the latent heat L changes by less than 1%. The largest effect of using the mean density and latent heat of vaporization is to reduce mean E by 1 W m^{-2} following the front.

The mean turbulent temperature scale (0.2K before the front) increases by a factor of 3 from the air temperature

maximum to its minimum and remains 30% higher an hour after the temperature minimum. Mean friction velocity u^* (0.2 m s^{-1} before the front) also increases dramatically in the mean, by 40% within the cold pool front, and by 10% for the hour following the front. The mean humidity scale q^* only increases 6% across the front.

The total mean fluxes are the sum of the product of the mean of the scales over all events (solid lines in Fig. 13a) and the covariances of u^* , T^* , and q^* among events (dashed lines in Fig. 13b). Variability among the cold pool events is mostly from variation of mean conditions over the longer than 2h surrounding them (Fig. 7). Rectified covariances among events do not vary

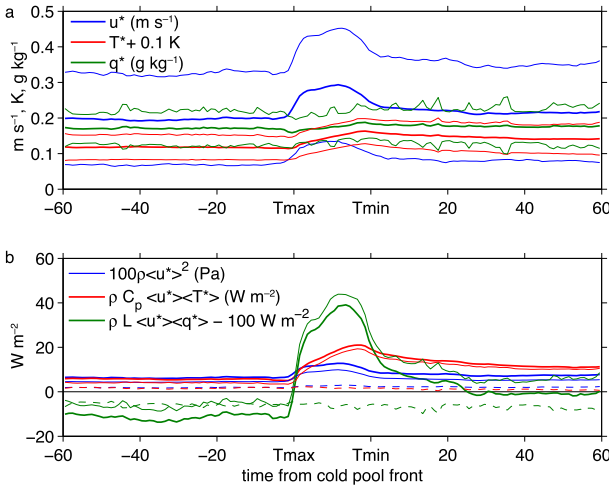


FIG. 13. Composite average (a) friction velocity u^* , temperature flux scale T^* , and specific humidity scale q^* within 1 h of the cold pool front. Thin lines indicate the standard deviation. (b) Flux composed as the product of mean u^* with mean u^* , T^* , or q^* (thin solid); interevent anomaly product (dashed) and full flux (thick solid).

systematically with the time relative to the cold front. The interevent wind stress covariance is $+2 \times 10^{-2}$ Pa, 30% of the total (Fig. 13b, blue dashed). Air is colder in windy events (Fig. 7), rectifying as a $+1.5 W m^{-2}$ sensible heat flux (Fig. 13b, red dashed), slightly higher before the front (when it is 30% of the total), and slightly lower after the front (10% of the total). Specific humidity is higher in windy events, so interevent humidity and wind variability rectifies into a nearly constant negative latent heat flux of $-6 W m^{-2}$ (Fig. 13b, green dashed).

b. Turbulent fluxes from eddy covariance

Turbulent stress, sensible heat flux, and latent heat flux are computed directly from covariances of fast (10Hz) velocity, temperature, and humidity anomalies with 3-, 6-, 12-, and 24-min windows (Fig. 14) from the NOAA/ESRL/Physical Science Division infrared water vapor analyzer, sonic anemometer, and accelerometer/angular rate sensor (ftp://ftp1.esrl.noaa.gov/psd3/cruises/DYNAMO_2011/Revelle/flux). Windows of each length start and end on t_{max} and t_{min} , the times of the temperature maximum and minimum associated with the front. Windows are tiled contiguously for 1 h previous to t_{max} and 1 h following t_{min} . Within the front, windows are tiled forward from t_{max} and backward from t_{min} to the midpoint of the front. (So the number of windows for each event depends on the duration of the front between t_{max} and t_{min} .) Fluxes are also computed for a second set of 24-min windows centered on t_{min} and

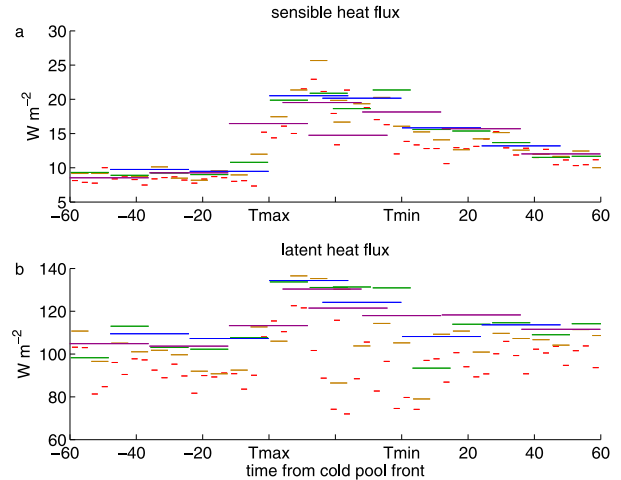


FIG. 14. Median (a) sensible and (b) latent direct covariance heat fluxes computed with 3- (red), 6- (tan), 12- (green), and 24-min (blue and purple) windows. Windows are tiled starting from t_{max} and t_{min} , except for the second (purple) set of 24-min windows, which are centered on t_{max} and t_{min} .

t_{max} . Medians of like window lengths and relative times are aggregated over all 211 events.

Surface fluxes are computed as covariances with vertical velocity, with the coordinate system rotated into the direction of the mean relative wind vector for each window. Platform motion is added to the velocity measured by the anemometer using complementary filtering (Edson et al. 1998). So that the window length corresponds exactly to the scale on which anomalies are defined, the anomalies are not detrended. (Tests show little dependence of the fluxes on detrending anomalies in each window.) Fluctuating temperature is solved from the sonic temperature and mean humidity (Schotanus et al. 1983), and sensible and latent heat fluxes are corrected for the mean velocity implied by mass conservation (Webb et al. 1980) in the appendix.

Fluxes are most enhanced at the front of the cold pool, between times t_{max} and t_{min} . From $9 W m^{-2}$ before the front, median sensible heat flux doubles in the front and remains 40% higher over the hour following the front. Median latent heat flux increases 20% from 105 to $130 W m^{-2}$ in the front and is $115 W m^{-2}$ following the front. The stronger response of the sensible heat flux reflects the observation that cold pools are cold and windy but not consistently drier than their surroundings. The short 6-min windows resolve $\sim 90\%$ of the sensible and latent heat flux. The latent heat flux by eddies longer than 6 min is about half as strong as the latent heat flux enhancement at the front. The sensible heat flux by eddies longer than 6 min is only about 5% as strong as the sensible heat flux enhancement at the front.

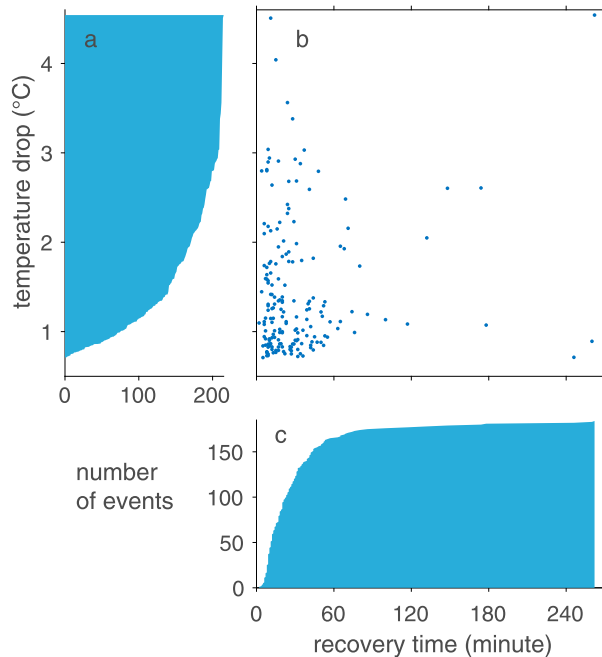


FIG. 15. (b) Scatterplot and (a),(c) cumulative distributions of cold pool temperature drop ΔT and recovery time τ .

Median turbulence covariance fluxes agree well with bulk fluxes computed with the COARE 3.5 algorithm (Fig. 13). Mean covariance fluxes are significantly larger than median fluxes over the events, so a few events with strong fluxes are disproportionately responsible for the mean flux. This helps explain the slightly lower flux changes reported here compared to the previous observational studies of Young et al. (1995) and Saxen and Rutledge (1998).

c. Cold pool recovery and depth

Surface air temperature and humidity recover gradually after the cold pool front passes. Figure 15 shows the recovery time scale estimated at the ship. The potential temperature of 181 of the 215 cold pools “recovered” when their temperature rose by $\Delta T/e$ within the cold pool. The remaining 34 cold pools had a temperature that did not recover by $\Delta T/e$ before encountering another cold pool (one encountered the end of the time series). The median recovery time scale was 20 min, although 2 cold pools approaching 5 h were detected (Fig. 15c). There is no correlation between cold pool strength ΔT and recovery time scale (Fig. 15b). Figure 6b shows the path distance of the wind within the $1/e$ recovery wake is usually quite short, with a median of 7 km.

Conservative variable analysis (Fig. 11) indicates the importance of entrainment of above-BL air to explain low specific humidity air observed at the surface. We

analyze the role of entrainment of boundary layer air in the mass and heat budget of the cold pool recovery. Sounding observations show that the potential temperature is adiabatic within the recovering cold pool and moist adiabatic above it, with little to no potential temperature jump between the layers. From this, we infer the mixed layer height h of the recovering cold pool as the height where the mixed-layer potential temperature θ meets the reference moist adiabat, $h = z_A + (\theta - \theta_A)/\Gamma$. The reference potential temperature $\theta_A(z_A)$ is temporally interpolated above the mixed layer from soundings, and Γ is the moist adiabatic lapse rate of potential temperature. The median cold pool depth was 320 ± 20 m when it initially encountered the ship. We find that the mixed-layer height grows at an average of 4 cm s^{-1} in the recoveries of 181 cold pools.

Using the mixed-layer depth h , we estimate the entrainment flux of potential temperature $\overline{w'\theta'_{\text{entr}}}$ in the wakes as a residual from the mixed-layer heat budget:

$$h(\partial\theta/\partial t) = \overline{w'\theta'_{\text{sfc}}} - \overline{w'\theta'_{\text{entr}}}. \quad (5)$$

Fluxes and tendencies are averaged over 10-min windows to reduce noise. Advection is neglected in (5). Advection would be cooling for cold surface air spreading out from the center of the cold pool, countering the temperature recovery. In this case the entrainment warming would be underestimated by the residual. Entrainment warming systematically exceeds the surface flux warming for the first 1.2 h of the recovery following the cold pool front (Fig. 16). The median entrainment flux is nearly 4 times larger than the surface flux in the first 10 min of the cold pool. Advection may be responsible for the negative “entrainment” residual for recoveries that persist longer than an hour. Average moisture entrainment, estimated in the same manner, has indeterminate sign, consistent with the finding that saturated downdrafts are not significantly moister or drier than the BL.

d. Cold pool dynamics

We assume that a hydrostatic pressure gradient acts to accelerate the cold pool front forward. The mean pressure increase of $\Delta p = p(t_{\text{min}}) - p(t_{\text{max}}) = 0.07 \pm 0.02$ hPa between two 60-s averages across the cold pool front is greater than the repeatability of the barometer measurement ($2\sigma = 0.03$ hPa for 1-s samples and 0.004 hPa for 1-min averages). Cold pools with $\Delta T < 1.1^\circ\text{C}$ do not have a significant pressure increase (Fig. 17). The strongest eight cold pools ($\Delta T > 3.0^\circ\text{C}$) have mean $\Delta p = 0.30 \pm 0.15$ hPa but are so few that their standard error

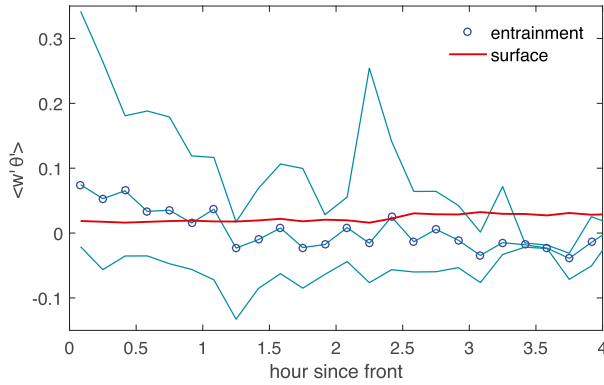


FIG. 16. Median surface flux (red) and 16th, 50th, and 84th percentiles of entrainment flux (blue), calculated as a residual from (5), as a function of time elapsed from t_{\min} .

overlaps the Δp for cold pools with intermediate ΔT . It is noteworthy that some of the surface-based cold pools are associated with pressure decreases. If the pressure is hydrostatic, this indicates a lighter column above the measurement point. Organized tropical convection is

capable of generating such conditions: for example, the mesolows accompanying squall lines (Zipser 1977).

The hydrostatic pressure anomaly at the surface across the front depends on the virtual temperature T'_v :

$$\frac{dp}{p} = -\frac{g}{R_d T'_v} dz \tag{6}$$

integrated over the depth of the anomaly. We expand the virtual temperature about the maximum virtual temperature before the cold pool $T_v = T_{v\max} + T'_v$, with the anomaly $T'_v \ll T_{v\max}$, so T'_v is zero before the cold pool. The anomaly at the front T'_v equals $T_{v\min} - T_{v\max}$ from the surface to h_{\min} and linearly decreases to zero at h_{\max} . The pressure anomaly is assumed to be zero at h_{\max} , and the pressure anomaly from T'_v is integrated downward. The mixed-layer heights h_{\max} and h_{\min} are from soundings, as in the previous section. The hydrostatic surface pressure change induced by the cold pool across the front is

$$\Delta p_{\text{hs}} = p_{\text{hs}}(t_{\min}) - p_{\text{hs}}(t_{\max}) = p(t_{\max}) \left\{ \exp \left[-\frac{g}{2R_d T_{v\max}^2} (T_{v\min} - T_{v\max})(h_{\min} - h_{\max}) \right] - 1 \right\}, \tag{7}$$

where the subscripts max and min refer to the times when T_{\max} and T_{\min} occurred.

There were 192 cold fronts for which the hydrostatic pressure increase could be computed (Fig. 18). Hydrostatic and observed pressure increases were $O(0.1)$ hPa. If a 0.1-hPa pressure change were distributed over 1 km, the resulting 10^{-3} m s^{-2} pressure gradient acceleration would obtain a velocity of 10 m s^{-1} if it were sustained unbalanced for 20 min. The hydrostatic pressure increase Δp_{hs} is weakly correlated ($r = 0.23$) to the observed pressure change Δp across the front. Given this low correlation, we conclude that the observed pressure has hydrostatic contributions from above the BL and/or non-hydrostatic contributions. The low correlation is comparable to the small anticorrelation of Δp and ΔT observed for several years of terrestrial cold pool passages over the Oklahoma Mesonet stations (Lesage 2013).

e. Cloud and rain evolution

Cold pools are supposed to originate from convection and to generate subsequent convection. To examine the temporal relationship between the DYNAMO cold pools and precipitation and clouds surrounding them, we composite the observations of

rain rate from an optical rain gauge on the ship and the liquid water and water vapor path observed by a microwave radiometer on the ship. Individual cold pool time series of rain ranked by the magnitude of their temperature drop ΔT are shown in Fig. 4. Rain is common and increases for cold pools with stronger temperature drops. Yet rain is not coincident with every cold pool, and though it is most likely to be stronger during the temperature front, rain may also be found before or after the front.

Rainy cold pools make up 141 of the cold pools (2/3 of the 211 for which rain gauge observations are available). The strongest rain, exceeding 10 mm h^{-1} , is centered on the cold pool front (Fig. 19a). The air temperature drops a few minutes before the rain, consistent with cold air flowing out ahead of the rain shower that generates it. Rain increases slightly (indicated by the third through sixth octiles) in the latter half of the front. Median rain rate is zero within minutes before and after the front and is more often observed following the front than before it. Mean rain rate increases from 0.5 to 2 mm h^{-1} after the front. Rain greater than $\sim 0.2 \text{ mm h}^{-1}$ is observed for 25% of cases for the hour following the cold pool front.

Cold pools sometimes spawn shallow cumulus in their wakes, which can be detected as liquid water

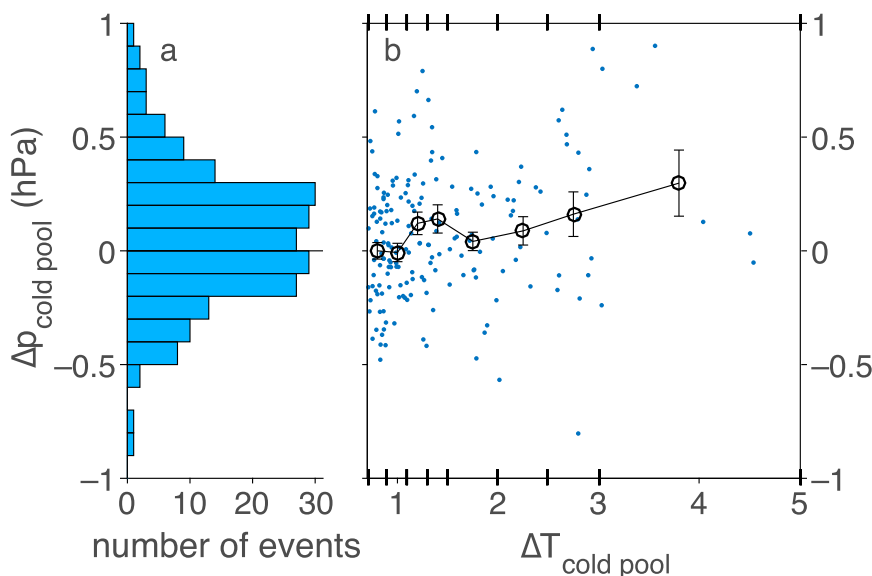


FIG. 17. (a) Histogram of pressure change observed across the cold pool. (b) Pressure change vs cold pool strength ΔT .

path (LWP) and water vapor path (WVP). Shallow cumulus clouds are common, but their small area is infrequently sampled directly overhead, resulting in small median liquid water paths (Fig. 19c). LWP and WVP are most enhanced after the front and rain maximum. In about 1/4 of the rainy cold pools, the LWP increases by about 1 kg m^{-2} in the coldest part of the wake. A saturated adiabatic shallow cumulus cloud of about 600 m from cloud base to cloud top would result in an LWP of 1 kg m^{-2} for conditions in DYNAMO. Vertically pointing cloud radar images corroborate the enhancement of shallow cumulus clouds. Synchronous with the LWP, WVP also increases by $>0.3 \text{ cm}$ for half of the rainy cold pools (Fig. 19b). The highest WVP and LWP near the minimum temperature of the cold pools are directly adjacent to times when rain was observed on the ship (Fig. 4). Masking times when the optical rain gauge observed rain (rate $> 1 \times 10^{-3} \text{ mm h}^{-1}$) excludes the highest WVP and LWP of the strongest cold pools and averages the only weaker, drier cold pools, but the timing of their maxima relative to the front is unchanged.

5. Summary

High-resolution (1-min average) time series detect and diagnose properties of a range of large to small cold pools. The evidence suggests that the observed small cold pools behave like the stronger longer-lasting cases observed in lower-resolution time series [e.g., COARE (Saxen and Rutledge 1998) and GATE (Barnes and

Garstang 1982)]. From the scales resolved, it appears that a fractal cascade of scales of cold pools is generated by the convective environment. Time series measurements at one point sample a number of fronts, but the age and history of each cold pool at the time it passes the ship is ambiguous. Cold pools spread and weaken as they age. A model for the strength, area, and age of cold pools would be useful to relate time series to the underlying populations of cold pools they sample.

A significant quantity of air must be entrained from the BL top (800 m) to keep the BL observed in DYNAMO both warmer than saturated downdrafts and drier than saturation at the sea surface temperature. Simulations show the sensible heat balance of the BL is mainly between -2 K day^{-1} each of evaporative and longwave cooling, and 4 K day^{-1} convergence of convective heat flux (Skylingstad and de Szoeke 2015). By mass, about one-half of the BL air mixture originates from entrainment, and one-fourth each from surface flux and saturated downdrafts, supporting the importance of entrainment for regulating BL moist static energy, as in the simulation of Thayer-Calder and Randall (2015).

On a shorter scale, entrainment mixing at the top of shallow cold pool wakes is responsible for the quick recovery of their temperature. Observed recovery times are much faster than estimates based on surface flux alone (e.g., Jorgensen et al. 1997; Ross et al. 2004). Entrainment flux in the cold pool recovery provides a sensible heating initially 4 times stronger than the surface heating. Moisture entrainment is not obvious.

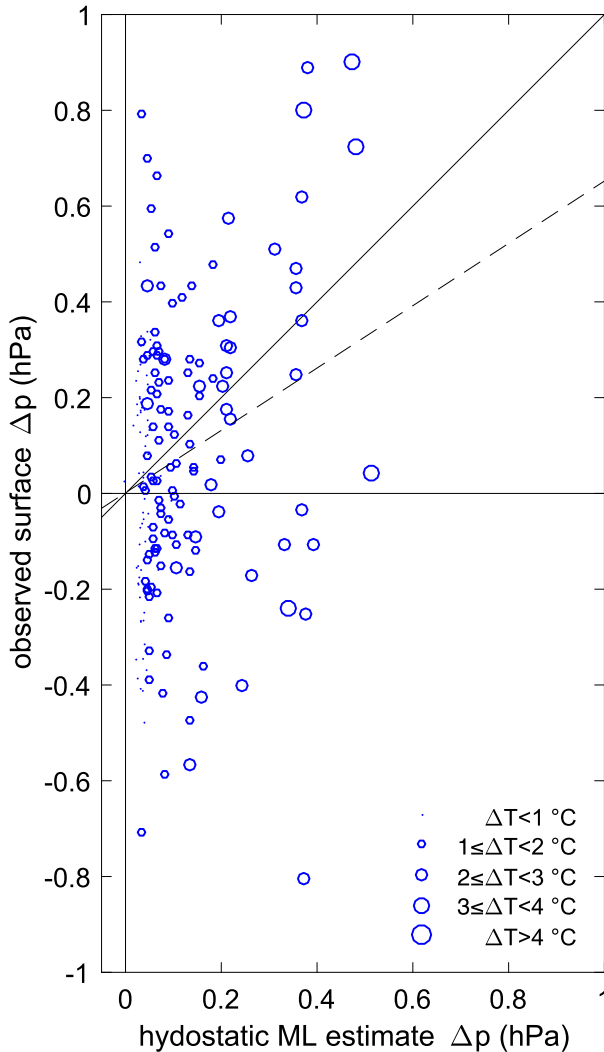


FIG. 18. Observed surface Δp vs Δp_{hs} computed from the temperature anomaly and estimates of the mixed-layer depth before and after the cold pool. Size of the circle indicates the strength ΔT of the cold pool. Thin lines indicate the origin and 1:1 line. The dashed line indicates the linear regression.

Vertical mixing of cold pools with their environment reduces their buoyancy anomaly also in tank experiments (Linden and Simpson 1986) and model simulations (Grant and van den Heever 2016).

Cold pools are slightly drier than their BL surroundings. Their humidity is similar to saturated downdrafts from the midtroposphere or air entrained from above the BL. They are drier than if unsaturated BL air were cooled in situ by rain falling and evaporating into the BL. These observations are consistent with model results that show moistening by rain evaporation to be small compared to the moistening sea surface evaporation.

The immediate effect of convective cold pools on BL air properties has been modeled using cloud-resolving

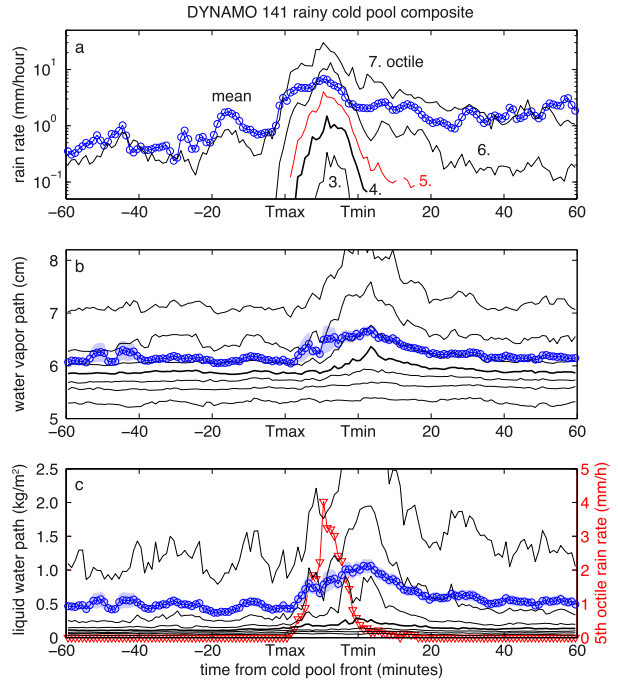


FIG. 19. (a) Composite mean (blue circles) and top five octiles (black, median is thick) of rain rate. Composite (b) water vapor path and (c) liquid water path mean (circles), standard error (shaded), and octiles. Red triangles show the fifth octile of rain rate in (b). The 141 rainy cold pools are composited.

models and large-eddy simulations (e.g., Tompkins 2001; Langhans and Romps 2015). In some of these simulations, positive water vapor anomalies form at the edges of cold pools, relative to the dry air injected at the center by the downdraft. Water vapor rings were first hypothesized to be due to the evaporation of rain into warm surface layer air (Tompkins 2001). More recent simulations attribute them to surface evaporation (Langhans and Romps 2015), and still others show that rain evaporation contributes significantly to the moistest air (Torri and Kuang 2016). Another explanation is convergence of preexisting moisture anomalies at the surface, perhaps associated with moisture in the original convection generating the cold pools. Preexisting moist patches can subsequently be lifted by cold pool dynamics (Li et al. 2014; Schlemmer and Hohenegger 2016). Observations of the marine tropical boundary layer are essential, not least because heat and moisture fluxes in the surface layer depend on parameterized subgrid turbulence and numerical diffusion in models, which may not faithfully resolve anomalies of the strong but shallow gradients of the surface layer associated with cold pools.

Surface moisture increased in GATE for rain rates greater than 2 mm h^{-1} , which Barnes and Garstang

(1982) attributed to rain evaporation because the MSE remained constant. Water vapor rings are not evident in observations from DYNAMO [this study or Yokoi et al. (2014)], COARE (Young et al. 1995; Saxen and Rutledge 1998), or RICO (Zuidema et al. 2012). The drying effect of entrainment on the BL, found here and in models (Thayer-Calder and Randall 2015), may explain why water vapor rings are rarely observed. From observations of moisture in cold pools and horizontal moisture fields from cloud-resolving model experiments with realistic winds (Feng et al. 2015; Skyllingstad and de Szoeke 2015), we hypothesize that air outside the cold pool is moister simply because it has had more time to equilibrate with the sea surface than the air in the cold pool. After a cold pool initially lowers the temperature and humidity at a surface point, the scalars recover gradually by surface fluxes toward equilibrium with the SST. Eventually, in a convective environment, the recovered relatively moist air is suddenly overtaken again by dry cold air from the next cold pool.

The properties of tropical marine boundary layers differ significantly from terrestrial boundary layers where dry convection and shear dominate exchange with the free troposphere. This study shows that convectively produced cold pools are one of the dominant processes controlling the temperature of the tropical marine BL. During periods of active convection, 30% of boundary layer air originates from saturated downdrafts. Current BL models based on downgradient mixing schemes may not accurately represent processes associated with convective downdrafts and cold pools.

Acknowledgments. We acknowledge J. Ruppert, E. Zipser, and an anonymous reviewer for helpful comments in the preparation of this paper; J. Edson for the University of Connecticut surface time series [Edson et al. (2016) (available at <ftp://dynamo.dms.uconn.edu/>); and the crew and our collaborators aboard the R/V *Revelle* during DYNAMO 2011. Collaborator A. Brewer provided useful visualizations and discussions of cold pools. L. Bariteau, J. Edson, J. Marion, and C. Fairall on the DYNAMO flux team measured the 10-Hz NOAA/ESRL/PSD turbulence flux time series, which is available online (ftp://ftp1.esrl.noaa.gov/psd3/cruises/DYNAMO_2011/Revelle/flux). Sounding data are provided by NCAR/EOL (Earth Observing Laboratory 2014). This work was supported by U.S. National Science Foundation Grants AGS-132189 and OCE-1129419, Office of Naval Research Grant N00014-10-1-0299, and National Oceanic and Atmospheric Administration Grants NA11OAR4310076, NA13OAR4310157, NA13OAR4310159, NA15OAR4310240, and NA15OAR4310242.

APPENDIX

Direct Covariance Heat Fluxes from Sonic Temperature and Water Vapor Density Fluctuations

The sonic anemometer measures sonic temperature T_s , and the infrared gas analyzer measures water vapor density ρ_v . The sonic temperature is related to the temperature T and water vapor specific humidity $q = \rho_v/\rho$ by

$$T_s = T(1 + \gamma q),$$

where the sonic water vapor coefficient γ is 0.51. The kinematic heat flux is related to the sonic temperature covariance with vertical velocity w :

$$\overline{w'T'} = \overline{w'T'_s} - \gamma T \overline{w'q'}. \quad (\text{A1})$$

Overbars indicate covariance averages of fast (primed) fluctuations. Unprimed quantities outside the covariance indicate means over the time scale of the covariance average.

The flux of virtual temperature $T_v = T(1 + \delta q)$, and hence density, resulting from temperature and water vapor flux requires a mean velocity in order to conserve mass (Webb et al. 1980) [$\delta = (1 - \epsilon)/\epsilon \approx 0.61$; $\epsilon = M_v/M_d$ is the ratio of molar masses of water to dry air]. They write the latent heat flux in terms of the water vapor density ρ_v :

$$\begin{aligned} E &= \rho_d L \overline{w'r'} = \rho L \overline{w'q'}/(1 - q) \\ &= L(1 + \sigma/\epsilon)(\overline{w'\rho'_v} + \rho_v \overline{w'T'/T}), \end{aligned} \quad (\text{A2})$$

with $\sigma = \rho_v/\rho_d = q/(1 - q)$. Substituting $\overline{w'q'}$ from the right-hand side of (A2) into (A1), the sensible heat flux H is written in terms of the observed fluctuations of sonic temperature and water vapor density:

$$\begin{aligned} H &= \rho c_p \overline{w'T'} \\ &= \rho c_p [1 + \gamma q(1 + \delta q)]^{-1} [\overline{w'T'_s} - \gamma T(1 + \delta q) \overline{w'\rho'_v}/\rho]. \end{aligned} \quad (\text{A3})$$

Substituting $\overline{w'T'}$ from (A3) into (A2) yields the latent heat flux

$$E = L(1 + \sigma/\epsilon) \left(\frac{1 - \alpha}{1 + \alpha} \overline{w'\rho'_v} + \frac{\rho_v}{T} \overline{w'T'_s} \right), \quad (\text{A4})$$

where $\alpha = \gamma q(1 + \delta q)$.

REFERENCES

Arakawa, A., and W. H. Schubert, 1974: Interaction of a cumulus cloud ensemble with the large-scale environment. Part I. *J. Atmos.*

- Sci.*, **31**, 674–701, doi:10.1175/1520-0469(1974)031<0674:IOACCE>2.0.CO;2.
- Barnes, G. M., and M. Garstang, 1982: Subcloud layer energetics of precipitating convection. *Mon. Wea. Rev.*, **110**, 102–117, doi:10.1175/1520-0493(1982)110<0102:SLEOPC>2.0.CO;2.
- Betts, A. K., 1976: The thermodynamic transformation of the tropical subcloud layer by precipitation and downdrafts. *J. Atmos. Sci.*, **33**, 1008–1020, doi:10.1175/1520-0469(1976)033<1008:TTTOT>2.0.CO;2.
- Chen, S. S., R. A. Houze, and B. E. Mapes, 1996: Multiscale variability of deep convection in relation to large-scale circulation in TOGA COARE. *J. Atmos. Sci.*, **53**, 1380–1409, doi:10.1175/1520-0469(1996)053<1380:MVODCI>2.0.CO;2.
- , and Coauthors, 2016: Aircraft observations of dry air, the ITCZ, convective cloud systems, and cold pools in MJO during DYNAMO. *Bull. Amer. Meteor. Soc.*, **97**, 405–423, doi:10.1175/BAMS-D-13-00196.1.
- de Szoeke, S. P., and J. B. Edson, 2017: Intraseasonal air–sea interaction and convection observed in DYNAMO/CINDY/AMIE. *The Global Monsoon System: Research and Forecast*, C. P. Chang, Ed., World Scientific, 349–364.
- , S. Yuter, D. Mechem, C. W. Fairall, C. D. Burleyson, and P. Zuidema, 2012: Observations of stratocumulus clouds and their effect on the eastern Pacific surface heat budget along 20°S. *J. Climate*, **25**, 8542–8567, doi:10.1175/JCLI-D-11-00618.1.
- , J. B. Edson, J. R. Marion, C. W. Fairall, and L. Bariteau, 2015: The MJO and air–sea interaction in TOGA COARE and DYNAMO. *J. Climate*, **28**, 597–622, doi:10.1175/JCLI-D-14-00477.1.
- Earth Observing Laboratory, 2014: R/V *Roger Revelle* radiosonde L3.1 data, version 1.0. Earth Observing Laboratory, accessed 26 May 2016, doi:10.5065/D6TH8K3Z.
- Edson, J. B., A. A. Hinton, K. E. Prada, J. E. Hare, and C. W. Fairall, 1998: Direct covariance flux estimates from mobile platforms at sea. *J. Atmos. Oceanic Technol.*, **15**, 547–562, doi:10.1175/1520-0426(1998)015<0547:DCFEFM>2.0.CO;2.
- , C. Fairall, and S. de Szoeke, 2016: R/V *Roger Revelle* flux, near-surface meteorology, and navigation data, version 3.0. Earth Observing Laboratory, accessed 13 December 2016, doi:10.5065/D6KPB80J9.
- Fairall, C. W., E. F. Bradley, J. S. Godfrey, G. A. Wick, J. B. Edson, and G. S. Young, 1996: Cool-skin and warm-layer effects on sea surface temperature. *J. Geophys. Res.*, **101**, 1295–1308, doi:10.1029/95JC03190.
- Feng, Z., S. A. McFarlane, C. Schumacher, S. Ellis, J. Comstock, and N. Bharadwaj, 2014: Constructing a merged cloud–precipitation radar dataset for tropical convective clouds during the DYNAMO/AMIE experiment at Addu Atoll. *J. Atmos. Oceanic Technol.*, **31**, 1021–1042, doi:10.1175/JTECH-D-13-00132.1.
- , S. Hagos, A. K. Rowe, C. D. Burleyson, M. N. Martini, and S. P. de Szoeke, 2015: Mechanisms of convective cloud organization by cold pools over tropical warm ocean during the AMIE/DYNAMO field campaign. *J. Adv. Model. Earth Syst.*, **7**, 357–381, doi:10.1002/2014MS000384.
- Grant, L. D., and S. C. van den Heever, 2016: Cold pool dissipation. *J. Geophys. Res. Atmos.*, **121**, 1138–1155, doi:10.1002/2015JD023813.
- Jabouille, P., J. L. Redelsperger, and J. P. Lafore, 1996: Modification of surface fluxes by atmospheric convection in the TOGA COARE region. *Mon. Wea. Rev.*, **124**, 816–837, doi:10.1175/1520-0493(1996)124<0816:MOSFBA>2.0.CO;2.
- Johnson, R. H., and M. E. Nicholls, 1983: A composite analysis of the boundary layer accompanying a tropical squall line. *Mon. Wea. Rev.*, **111**, 308–319, doi:10.1175/1520-0493(1983)111<0308:ACAOTB>2.0.CO;2.
- , and P. E. Ciesielski, 2013: Structure and properties of Madden–Julian oscillations deduced from DYNAMO sounding arrays. *J. Atmos. Sci.*, **70**, 3157–3179, doi:10.1175/JAS-D-13-065.1.
- Jorgensen, D. P., M. A. LeMone, and S. B. Trier, 1997: Structure and evolution of the 22 February 1993 TOGA COARE squall line: Aircraft observations of precipitation, circulation, and surface energy fluxes. *J. Atmos. Sci.*, **54**, 1961–1985, doi:10.1175/1520-0469(1997)054<1961:SAEOTF>2.0.CO;2.
- Kerns, B. W., and S. S. Chen, 2014: Equatorial dry air intrusion and related synoptic variability in MJO initiation during DYNAMO. *Mon. Wea. Rev.*, **142**, 1326–1343, doi:10.1175/MWR-D-13-00159.1.
- Kingsmill, D. E., and R. A. Houze, 1999: Thermodynamic characteristics of air flowing into and out of precipitating convection over the west Pacific warm pool. *Quart. J. Roy. Meteor. Soc.*, **125**, 1209–1229, doi:10.1002/qj.1999.49712555606.
- Langhans, W., and D. M. Romps, 2015: The origin of water vapor rings in tropical oceanic cold pools. *Geophys. Res. Lett.*, **42**, 7825–7834, doi:10.1002/2015GL065623.
- Lee, H.-T., 2014: Climate Algorithm Theoretical Basis Document (C-ATBD): Outgoing longwave radiation (OLR)—Daily. NOAA’s Climate Data Record Program Tech. Doc. CDRP-ATBD-0526, 46 pp. [Available online at <http://www1.ncdc.noaa.gov/pub/data/sds/cdr/CDRs/Outgoing%20Longwave%20Radiation%20-%20Daily/AlgorithmDescription.pdf>.]
- LeMone, M. A., and E. J. Zipser, 1980: Cumulonimbus vertical velocity events in GATE. Part I: Diameter, intensity and mass flux. *J. Atmos. Sci.*, **37**, 2444–2457, doi:10.1175/1520-0469(1980)037<2444:CVVEIG>2.0.CO;2.
- Lesage, A. T., 2013: Frontal passage and cold pool detection using Oklahoma Mesonet observations. M.S. thesis, Dept. of Atmospheric Sciences, University of Utah, 85 pp.
- Li, Z., P. Zuidema, and P. Zhu, 2014: Simulated convective invigoration processes at trade wind cumulus cold pool boundaries. *J. Atmos. Sci.*, **71**, 2823–2841, doi:10.1175/JAS-D-13-0184.1.
- Linden, P. F., and J. E. Simpson, 1986: Gravity-driven flows in a turbulent fluid. *J. Fluid Mech.*, **172**, 481–497, doi:10.1017/S0022112086001829.
- Lucas, C., E. J. Zipser, and M. A. Lemone, 1994: Vertical velocity in oceanic convection off tropical Australia. *J. Atmos. Sci.*, **51**, 3183–3193, doi:10.1175/1520-0469(1994)051<3183:VVIOCO>2.0.CO;2.
- Mapes, B. E., and P. Zuidema, 1996: Radiative–dynamical consequences of dry tongues in the tropical troposphere. *J. Atmos. Sci.*, **53**, 620–638, doi:10.1175/1520-0469(1996)053<0620:RDCODT>2.0.CO;2.
- Matthews, A. J., D. B. Baranowski, K. J. Heywood, P. J. Flatau, and S. Schmidtko, 2014: The surface diurnal warm layer in the Indian Ocean during CINDY/DYNAMO. *J. Climate*, **27**, 9101–9122, doi:10.1175/JCLI-D-14-00222.1.
- Moum, J. N., and Coauthors, 2014: Air–sea interactions from westerly wind bursts during the November 2011 MJO in the Indian Ocean. *Bull. Amer. Meteor. Soc.*, **95**, 1185–1199, doi:10.1175/BAMS-D-12-00225.1.
- Raymond, D. J., 1994: Convective processes and tropical atmospheric circulations. *Quart. J. Roy. Meteor. Soc.*, **120**, 1431–1455, doi:10.1002/qj.49712052002.
- Rio, C., F. Hourdin, J. Y. Grandpeix, and J. P. Lafore, 2009: Shifting the diurnal cycle of parameterized deep convection over land. *Geophys. Res. Lett.*, **36**, L07809, doi:10.1029/2008GL036779.
- Ross, A. N., A. M. Tompkins, and D. J. Parker, 2004: Simple models of the role of surface fluxes in convective cold pool evolution. *J. Atmos. Sci.*, **61**, 1582–1595, doi:10.1175/1520-0469(2004)061<1582:SMOTRO>2.0.CO;2.

- Rowe, A. K., and R. A. Houze, 2015: Cloud organization and growth during the transition from suppressed to active MJO conditions. *J. Geophys. Res. Atmos.*, **120**, 10324–10350, doi:[10.1002/2014JD022948](https://doi.org/10.1002/2014JD022948).
- Saxen, T. R., and S. A. Rutledge, 1998: Surface fluxes and boundary layer recovery in TOGA COARE: Sensitivity to convective organization. *J. Atmos. Sci.*, **55**, 2763–2781, doi:[10.1175/1520-0469\(1998\)055<2763:SFABLR>2.0.CO;2](https://doi.org/10.1175/1520-0469(1998)055<2763:SFABLR>2.0.CO;2).
- Schlemmer, L., and C. Hohenegger, 2014: The formation of wider and deeper clouds as a result of cold-pool dynamics. *J. Atmos. Sci.*, **71**, 2842–2858, doi:[10.1175/JAS-D-13-0170.1](https://doi.org/10.1175/JAS-D-13-0170.1).
- , and —, 2016: Modifications of the atmospheric moisture field as a result of cold-pool dynamics. *Quart. J. Roy. Meteor. Soc.*, **142**, 30–42, doi:[10.1002/qj.2625](https://doi.org/10.1002/qj.2625).
- Schotanus, P., F. T. M. Nieuwstadt, and H. A. R. De Bruin, 1983: Temperature measurement with a sonic anemometer and its application to heat and moisture fluxes. *Bound.-Layer Meteor.*, **26**, 81–93, doi:[10.1007/BF00164332](https://doi.org/10.1007/BF00164332).
- Skyllingstad, E. D., and S. P. de Szoeke, 2015: Cloud-resolving large-eddy simulation of tropical convective development and surface fluxes. *Mon. Wea. Rev.*, **143**, 2441–2458, doi:[10.1175/MWR-D-14-00247.1](https://doi.org/10.1175/MWR-D-14-00247.1).
- Thayer-Calder, K., and D. Randall, 2015: A numerical investigation of boundary layer quasi-equilibrium. *Geophys. Res. Lett.*, **42**, 550–556, doi:[10.1002/2014GL062649](https://doi.org/10.1002/2014GL062649).
- Tompkins, A. M., 2001: Organization of tropical convection in low vertical wind shears: The role of cold pools. *J. Atmos. Sci.*, **58**, 1650–1672, doi:[10.1175/1520-0469\(2001\)058<1650:OOTCIL>2.0.CO;2](https://doi.org/10.1175/1520-0469(2001)058<1650:OOTCIL>2.0.CO;2).
- Torri, G., 2016: A Lagrangian study of precipitation-driven downdrafts. *J. Atmos. Sci.*, **73**, 839–854, doi:[10.1175/JAS-D-15-0222.1](https://doi.org/10.1175/JAS-D-15-0222.1).
- , and Z. Kuang, 2016: Rain evaporation and moist patches in tropical boundary layers. *Geophys. Res. Lett.*, **43**, 9895–9902, doi:[10.1002/2016GL070893](https://doi.org/10.1002/2016GL070893).
- Webb, E. K., G. I. Pearman, and R. Leuning, 1980: Correction of flux measurements for density effects due to heat and water vapour transfer. *Quart. J. Roy. Meteor. Soc.*, **106**, 85–100, doi:[10.1002/qj.49710644707](https://doi.org/10.1002/qj.49710644707).
- Wheeler, M. C., and H. H. Hendon, 2004: An all-season real-time multivariate MJO index: Development of an index for monitoring and prediction. *Mon. Wea. Rev.*, **132**, 1917–1932, doi:[10.1175/1520-0493\(2004\)132<1917:AARMMI>2.0.CO;2](https://doi.org/10.1175/1520-0493(2004)132<1917:AARMMI>2.0.CO;2).
- Yokoi, S., M. Katsumata, and K. Yoneyama, 2014: Variability in surface meteorology and air–sea fluxes due to cumulus convective systems observed during CINDY/DYNAMO. *J. Geophys. Res. Atmos.*, **119**, 2064–2078, doi:[10.1002/2013JD020621](https://doi.org/10.1002/2013JD020621).
- Yoneyama, K., C. Zhang, and C. N. Long, 2013: Tracking pulses of the Madden–Julian oscillation. *Bull. Amer. Meteor. Soc.*, **94**, 1871–1891, doi:[10.1175/BAMS-D-12-00157.1](https://doi.org/10.1175/BAMS-D-12-00157.1).
- Young, G. S., S. M. Perugini, and C. W. Fairall, 1995: Convective wakes in the equatorial western Pacific during TOGA. *Mon. Wea. Rev.*, **123**, 110–123, doi:[10.1175/1520-0493\(1995\)123<0110:CWITEW>2.0.CO;2](https://doi.org/10.1175/1520-0493(1995)123<0110:CWITEW>2.0.CO;2).
- Zhang, G. J., and N. A. McFarlane, 1995: Sensitivity of climate simulations to the parameterization of cumulus convection in the Canadian Climate Centre General Circulation Model. *Atmos.–Ocean*, **33**, 407–446, doi:[10.1080/07055900.1995.9649539](https://doi.org/10.1080/07055900.1995.9649539).
- Zipser, E. J., 1969: The role of organized unsaturated convective downdrafts in the structure and rapid decay of an equatorial disturbance. *J. Appl. Meteor.*, **8**, 799–814, doi:[10.1175/1520-0450\(1969\)008<0799:TROUC>2.0.CO;2](https://doi.org/10.1175/1520-0450(1969)008<0799:TROUC>2.0.CO;2).
- , 1977: Mesoscale and convective-scale downdrafts as distinct components of squall-line structure. *Mon. Wea. Rev.*, **105**, 1568–1589, doi:[10.1175/1520-0493\(1977\)105<1568:MACDAD>2.0.CO;2](https://doi.org/10.1175/1520-0493(1977)105<1568:MACDAD>2.0.CO;2).
- Zuidema, P., and Coauthors, 2012: On trade wind cumulus cold pools. *J. Atmos. Sci.*, **69**, 258–280, doi:[10.1175/JAS-D-11-0143.1](https://doi.org/10.1175/JAS-D-11-0143.1).